Hybrid QM/MM free energy evaluation of drug-resistant mutational effect on binding of an inhibitor Indinavir to HIV-1 protease

Masahiko Taguchi[1,2], Ryo Oyama[1], Masahiro Kaneso[1], and Shigehiko Hayashi[1*]

[1]*Department of Chemistry, Graduate School of Science, Kyoto University, Kyoto 606-8502, Japan*

[2]*Institute for Quantum Life Science, National Institutes for Quantum Science and Technology, Kizugawa, Kyoto 619-0215, Japan*

Email: hayashig@kuchem.kyoto-u.ac.jp, Phone: +81-75-753-4006, and Fax: +81-75-753-4000

ABSTRACT

Human immunodeficiency virus 1 (HIV-1) protease is a homo-dimeric aspartic protease essential for replication of HIV. The HIV-1 protease is a target protein in drug discovery for antiretroviral therapy, and various inhibitor molecules of transition state analog were developed. However, serious drug-resistant mutants have emerged. For understanding molecular mechanism of the drug-resistance, accurate examination of the impacts of the mutations on ligand binding as well as enzymatic activity is necessary. Here, we present a molecular simulation study on the ligand binding of Indinavir, a potent transition state analog inhibitor, to the wild-type protein and a V82T/I84V drug-resistant mutant of HIV-1 protease. We employed a hybrid ab initio quantum mechanical/molecular mechanical (QM/MM) free energy optimization technique which combines highly accurate QM description of the ligand molecule and its interaction with statistically ample conformational sampling of MM protein environment by long-time molecular dynamics simulations. Through free energy calculations of protonation states of catalytic groups at the binding pocket and of ligand binding affinity changes upon the mutations, we successfully reproduced the experimentally observed significant reduction of the binding affinity upon the drug-resistant mutations and elucidated the underlying molecular mechanism. The present study opens the way for understanding the molecular mechanism of drug-resistance through direct quantitative comparison of ligand binding and enzymatic reaction with the same accuracy.

2

INTRODUCTION

Human immunodeficiency virus 1 (HIV-1) protease functions in maturation of HIV particles. The protease site-specifically cleavages peptide bonds of polyproteins of HIV through catalytic hydrolysis reactions. Since the protease-mediated maturation is essential for virus infectivity, HIV-1 protease is a target protein for drug discovery and various inhibitors that block its protease activity have been developed [1,2]. HIV-1 protease forms a homo-dimer composed of monomers denoted as A and B, respectively. Despite the C_2 symmetry of the protein complex, the monomers A and B become distinguishable upon the binding of asymmetric peptide substrates and inhibitor molecules. The catalytic site is located at the dimer interface (Figures 1 and S1). Two aspartic acids at the positions of 25, Asp25(A) and Asp25(B), in the catalytic site act as the catalytic groups for the hydrolysis reactions of the peptide bonds [3,4].

Inhibitors for HIV-1 protease mainly developed so far are characterized as transition state analogs [1,5,6]. Because the transition state of an enzymatic reaction is energetically stabilized for catalytic activity, the inhibitor molecule that mimics the transition state structure of the enzyme's wild-type substrate is expected to be bound to the enzyme more strongly than the substrate in the reactant and product states. An inhibitor, Indinavir (Figures 1 and 2), is one of such transition state analogs [7-15]. Indinavir possesses an sp^3 secondary alcohol structure, instead of an sp^2 carbonyl one in the wild-type peptide substrate, at the cleavage site in the vicinity

3

of the catalytic Asp25 groups. The secondary alcohol structure of Indinavir mimics a diol form in the transition state of the wild-type substrate where a lytic water molecule is attacking. Together with bulky groups analogous to hydrophobic residues at the cleavage sites of the HIV polyprotein such as Pro-Phe, Met-Met, and Leu-Ala [16,17], Indinavir is tightly bound to the catalytic site of HIV-1 protease and in turn potently inhibits its enzymatic activity.

However, serious antiviral drug-resistances to HIV-1 protease inhibitors including Indinavir have emerged [1,2,13,14,18-28]. Among the drug-resistant mutations, the V82T/I84V mutation greatly decreases the binding affinity of Indinavir (60- to 70-fold increase of the dissociation constant), while no significant structural changes by the mutation from the wild-type one (C_α–RMSD $\sim$ 0.2 Å) were observed by an X-ray crystallographic experiment [12]. In addition, reductions of the catalytic activities of the mutant for some of the cleavage sites of the polyprotein remain much more modest [14], giving rise to the drug-resistance. Note that, if the transition state analog inhibitor literally mimicked the wild-type substrate in the transition state, the mutation that reduces the binding affinity of the inhibitor also depressed the enzymatic activity of the mutant to a similar extent and thus abolished the drug-resistant behavior. Hence, the inhibitor that is expected to be tolerantly effective against mutations is a compound that well captures the chemical nature of the wild-type substrate in the transition state. For molecular design of such an inhibitor tolerant to drug-resistance, therefore, simultaneous examinations of the inhibitor binding

and the enzymatic activity of the wild-type substrate are necessary.

For understanding and design of the inhibitor binding, determination of protonation state of the key catalytic carboxyl groups, Asp25, is also necessary. Difference in the protonation state strongly alters electrostatic environment at the interface between the protein and the inhibitor, and thus significantly affects nature of their binding interaction. However, because hydrophobic groups of Indinavir fill space around Asp25 in the binding form [12], electrostatic environment around Asp25 in the inhibitor binding state is significantly different from that in the protein without the inhibitor binding. Furthermore, as the asymmetric peptide substrate and the inhibitor molecule breaks the C_2 symmetry of the homo-dimer HIV-1 protease upon their bindings as described above, the protonation states of the two carboxylic acids of Asp25 in the homo-dimer proteins can differ depending on the substrate and inhibitor molecules bound despite that the proteins are sequentially symmetric.

Although the protonation states for the wild-type substrate and some inhibitors were measured experimentally by biochemical, NMR, and neutron diffraction techniques [29-35], protonation states for the proteins with various inhibitors are not sufficiently examined. Theoretical determination of the protonation states is also a formidable task because the protonation changes a charge of the group and thus evaluation of the free energy associated with the protonation requires high accuracy of the electronic states of the chemical bond formation as well as large

electrostatic reorganization of the extensive protein environment. In fact, despite that many

theoretical investigations on the protonation states were performed until now [36-50], consensus

on the protonation state for the protein binding Indinavir is seemingly yet to be reached because

of their discrepancy (Table S1) [37,38,41,42,45].

Here, we present a hybrid molecular simulation study on Indinavir bound to HIV-1 protease

and its drug-resistant V82T/I84V mutant. As described above, although HIV-1 protease and its

drug resistant mutants are extensively studied experimentally [1-35] and computationally [36-56],

the microscopic molecular mechanism underlying the drug resistance is not well understood yet.

To develop a methodology to tackle the problem, a test system which has been well-characterized

experimentally is necessary. Since the biochemical and structural properties of HIV-1 protease

have extensively been examined experimentally, HIV-1 protease is one of the best systems for

the present purpose of elucidating the molecular mechanism underlying the drug resistance.

To theoretically examine the inhibitor binding process, we employed a hybrid quantum

mechanical/molecular mechanical (QM/MM) free energy method called the QM/MM

reweighting free energy-self-consistent field (RWFE-SCF) method [57,58]. The method

combines highly accurate ab initio QM calculations for a reaction center with long-time molecular

dynamics (MD) simulations using MM force fields for an extended protein system in fully

variational and computationally efficient manners, allowing one to properly describe mechanistic

coupling of a complex chemical event at the reaction center with global conformational changes

of the protein system. The method was thus utilized for ab initio evaluation of a free energy

activation energy of an enzymatic reaction [57,59] as well as structural modeling and design of

photo-receptor proteins [60-63]. Especially, the method successfully predicted functional

conformational changes of the proteins upon a photo-chemical reaction and mutations, which

were later experimentally confirmed by X-ray crystallographic measurements [60,64], showing a

high reliability of molecular modeling of a protein with a chemically complex ligand compound

and its mutants.

In the present study, we treated the whole molecule of Indinavir and the catalytic sidechains of

Asp25 quantum mechanically. The advantage of the QM/MM simulation approach over a

simulation only with MM force fields is three-fold. First, the quantum treatment avoids difficulty

in developing an accurate force field of ligand molecules. Although several efficient and accurate

schemes for parameterizing classical MM force fields for small ligand molecules have been

proposed [65,66], it is not obvious that classical force fields are accurate enough to describe

structures and energies of small ligand molecules in proteins. Especially, in the present system,

Indinavir hydrogen-bonds with a possibly anionic sidechain(s) of deprotonated Asp25, which, for

accurate evaluation of structure and energetics, requires description of electronic polarization and

charge transfer interactions absent in conventional MM force fields. Furthermore, Indinavir

exhibits several intramolecular interactions of hyperconjugation (intramolecular electronic delocalization between adjacent σ and π orbitals) for which the QM treatment provides essentially more accurate description.

An apparent shortcoming of a conventional QM/MM MD simulation, which is able to treat the molecular interactions quantum mechanically, for a ligand binding problem is its considerably demanding computational costs which preclude long-time MD simulations for sufficient statistical sampling. However, the present approach of the QM/MM RWFE-SCF method enables optimizations of electronic wavefunction and structure of the reaction center and the ligand binding site described quantum chemically on an extensive free energy surface of the protein environment obtained by long-time MD simulations with MM force fields, and thus partly overcomes the difficulty of conventional QM/MM MD simulations in obtaining sufficient statistical conformational samples.

Second, the protonation states of Asp25 can be determined to properly evaluate the binding affinity of the inhibitor as described above. Since the protonation of the carboxyl group involves chemical bond formation and dissociation, the QM/MM treatment is a straightforward and accurate approach. It is again noteworthy that the QM/MM RWFE-SCF method employed in the present study is capable of sufficiently sampling conformational changes of the protein environment representing reorganization in response to significant change of electrostatic

potential upon the protonation change by the long-time MD simulations with MM force fields in the QM/MM optimization procedure.

Finally, to understand the molecular mechanism of drug resistance, the method allows one to treat both of the ligand binding process and the enzymatic reaction one. For the latter, one inevitably needs to employ the QM/MM approach as the chemically active transition state determines the enzymatic activity. It is therefore preferable to employ the same QM/MM approach for the ligand binding process as well, which avoids introducing a possible error due to use of computationally different methods.

In the present study, we first identified the protonation states of Asp25 for both the wild-type protein and the V82T/I84V mutant binding Indinavir by QM/MM RWFE-SCF free energy optimizations and free energy perturbation calculations. We found that water hydration to the symmetric carboxyl groups of Asp25 in the homo-dimer is asymmetric, which determined the protonation states of Asp25. We then calculated a difference in binding free energy of the inhibitor between the wild-type protein and the mutant by alchemical free energy perturbation calculations [54,67-74]. The QM/MM calculation successfully reproduced the significant reduction of the binding free energy of the inhibitor upon the V82T/I84V mutation, which was not well described by the simulation only with the MM force fields. The QM/MM approach which enables the evaluation of the effect of drug-resistant mutations on the inhibitor binding opens the way for

understanding of the molecular mechanism of the drug-resistance.

COMPUTATIONAL METHODS

To describe conformational and energetic couplings of the ligand binding with slow and extensive thermal relaxation of the wild-type protein and its mutant, we employed the QM/MM RWFE-SCF method by which the molecular geometry of the QM part is optimized at the ab initio level of theory on an extensive mean-field free energy surface constructed from statistical samples of the MM part generated by long-time MD simulations [57,58]. Free energy differences between the optimized states on the free energy surface were then calculated by MD simulations with a free energy perturbation (FEP) method [59]. Furthermore, free energy changes upon the drug-resistant mutations were evaluated by alchemical MD simulations. The details of the QM/MM RWFE-SCF calculations and the MD simulations were described below and in Supporting Information. All the QM/MM calculations and the MD simulations were performed with GAMESS2014 [75] with locally implemented QM/MM codes, and pmemd.cuda of AMBER16 [76,77] except for alchemical free energy calculations, which was performed that of AMBER18 [77,78], respectively.

QM/MM RWFE-SCF method. Figure 3 depicts calculation scheme of the QM/MM RWFE-SCF free energy optimization. In the optimization procedure of the method, iterative calculations of the long-time MD samplings of the MM part constructing the free energy surface and the ab initio QM/MM geometry optimizations of the QM part on the free energy surface are carried out

until simultaneous convergences of the QM geometry optimization and the MD statistical sampling are achieved. The iterative procedure of the optimization is called the sequential sampling [79].

After preparatory steps to obtain the initial structure and parameters of the simulation system, the iterative cycles of the sequential sampling are started. Each iterative cycle consists of an MD sampling calculation of the MM part for 10 ns and a QM/MM geometry optimization of the QM part with the conformational samples of the MM part. In the former MD sampling calculation, a trajectory calculation with fixed geometry and effective atomic charges of the QM part determined in the previous cycle is performed and 50,000 MM conformations are obtained from the last half of the trajectory for 5 ns. The latter QM/MM geometry optimization is then performed on a mean-field free energy surface of those sampled MM conformations using mean energy gradients, and the geometry and effective atomic charges of the QM part are updated for the next cycle of the sequential sampling. The QM/MM geometry optimization procedure is designed to be theoretically variational and computationally highly efficient by introducing a statistical reweighting scheme and the restrained electrostatic potential (RESP) operator of the QM-MM electrostatic interaction [57,58]. Finally, the overall convergence of the sequential sampling is evaluated by the simultaneous convergences of the QM/MM geometry optimization and the statistics of the MM ensemble, in the latter of which the most of the conformational samples well

contribute to the average of the QM-MM interaction even in the statistical reweighting.

MD simulations. The initial structure of the protein binding Indinavir was constructed based

on an X-ray crystallographic structure (PDB ID: 1HSG, UniProt ID: P03367) [12]. We then

replaced several amino acids so that the amino acid sequence is identical to that of an X-ray

crystallographic structure of HIV-1 protease binding an inhibitor, JE-2147, (PDB ID: 1KZK,

UniProt ID: P03369) [80], which we employed in another ongoing study on the enzymatic

catalysis, allowing a direct comparison of the effects of the drug-resistant mutations on the

binding of Indinavir and the enzymatic catalysis. The amino acids replaced are located on surface

of the protein far from the binding pocket and C_α-RMSD between those X-ray crystallographic

structures of two HIV-1 proteases is small (0.60 Å) (Figure S2). Thus, the amino acids replaced

are considered functionally minor. We followed the definition of the chains A and B in the X-ray

crystallographic structure of HIV-1 protease binding Indinavir (PDB ID: 1HSG) [12].

We modeled two mono-protonated states, AH and BH, where either the catalytic aspartate

Asp25(A) or Asp25(B) is protonated, respectively, because those two aspartic acids are

experimentally known to be generally mono-protonated in the case of asymmetric type inhibitors

[31-35]. The protonation state of Indinavir is assumed to be neutral based on experimental

observation [81,82]. Although Indinavir includes a piperazine group of which pK_a is higher than

7 in water, the piperazine part is surrounded by hydrophobic residues in the binding pocket of

HIV-1 protease (Figure S3) [4,12], and thus its pK_a is expected to be largely reduced when it is bound to HIV-1 protease. In fact, the amino acids in the native substrate of which position corresponds to the piperazine group in Indinavir are neutral hydrophobic ones (Figure S3) [4,14,22].

Each protein was immersed in a nearly cubic boxes (96.1 × 96.3 × 96.1 Å^3) in a periodic boundary condition filled with TIP3P water molecules [83] and seven Cl$^-$ ions were added to neutralize the system. The total number of atoms in the box was 76,041 (Figure 1b). The AMBER ff14SB parameter set [84] and the parameter set reported in Ref. [85] were employed for the force fields of the protein and the Cl$^-$ ions, respectively. The force field parameters of Indinavir were taken from AMBER parameter database [42] and GAFF [65]. We also modeled the simulation systems of the V82T/I84V mutant based on those of the wild-type. Details of the modeling are given in Supporting Information.

Prior to the QM/MM RWFE-SCF simulations, equilibrium MD simulations with the fully MM classical simulations at 300 K for 1 μs in NPT condition were carried out (see Supporting Information).

QM/MM RWFE-SCF free energy optimizations. The QM regions consisted of Indinavir and the sidechains of Asp25(A) and Asp25(B) (Figure 2). The dangling bonds at the boundaries of the QM and MM regions were capped with dummy hydrogen atoms. The total number of the QM

atoms were 105. The density functional theory (DFT) method with B3LYP-D3 functional [86,87]

and 6-31G** basis set was used, except for the two carboxyl groups of Asp25 where 6-31+G**

basis set was employed, and for the boundary atoms, the hydrogen atoms connecting to the

boundary ones, and the dummy hydrogen atoms where 6-31G basis set was used. The total

number of the basis functions were 1,059. The MD sampling calculations were performed in NVT

ensemble condition.

The free energy geometry optimizations for the protonation states AH and BH of the wild-type

required 110 and 159 cycles (i.e., the MD sampling simulations for 1.10 and 1.59 μs in total),

respectively. In the case of the free energy optimization of the V82T/I84V mutant system initially

in the BH protonation state, the proton at Asp25(B) was spontaneously transferred to Asp25(A)

around at 5th cycle of the sequential samplings and stayed in the AH protonation state after the

proton transfer (see below). The free energy geometry optimizations required 96 and 147 cycles

for the systems in the initial protonated states, AH and BH, respectively (MD simulations for 0.96

and 1.47 μs in total). For the evaluation of the free energy difference between the AH and BH

protonation states of the V82T/V84V mutant, we also performed a QM/MM RWFE-SCF free

energy optimization of the mutant in the BH state by imposing constraint to fix bond distance

between $O_{\delta2}$ and $H_{\delta2}$ atoms of Asp25(B) at 1.07 Å in order to prevent the spontaneous proton

transfer to Asp25(A). The constraint free energy optimization in the BH state finished at 95 cycles

(MD simulations for 0.95 μs in total).

The QM/MM optimized structures and the energies of the AH state, which was shown to be energetically more stable than the BH one (see below), were also determined by QM/MM RWFE-SCF free energy optimizations with DFT M06-2X functional [88] from those obtained with DFT B3LYP-D3 functional. The free energy geometry optimizations required 119 and 170 cycles of the sequential samplings for the wild-type protein and the V82T/I84V mutant, respectively (MD simulations for 1.19 and 1.70 μs in total).

Equilibrium MD simulations of the AH systems of which the geometry and the effective atomic charges of the QM region were fixed at the QM/MM free energetically optimized ones for 1 μs each were then carried out for analysis of the protein conformations.

Evaluation of free energy differences between AH and BH protonation states. To energetically characterize the AH and BH protonation states, free energy differences between those protonation states were evaluated by FEP calculations as described previously [59]. The free energy differences between the optimized states X and Y are given as

$$\Delta_{Y\text{-}X}F_{QM/MM} = \Delta_{Y\text{-}X}E_{QM} + \Delta_{Y\text{-}X}F_{QM\text{-}MM,MM} \tag{1}$$

where $\Delta_{Y\text{-}X}E_{QM}$ is the difference between the expectation values of the QM Hamiltonian and $\Delta_{Y\text{-}X}F_{QM\text{-}MM,MM}$ is the free energy difference originating from QM-MM interactions and MM interactions in the MM region. The former was directly obtained by the QM/MM RWFE-SCF

16

free energy optimization, while the latter was evaluated with the FEP method with Bennett acceptance ratio (BAR) [89-91].

For the FEP calculation, the geometry and the effective atomic charges of the QM region were changed with linearly divided discrete 20 points. The MD simulation at each point was started from the last snapshot of the MD trajectory calculation at the previous point. Both of the forward calculation where AH was changed to BH (denoted AH → BH) and the backward one where BH was changed to AH (denoted BH → AH) were performed to assess the statistical convergence. The total length of the MD trajectory calculation is 1 μs each.

MD Simulation for inhibitor unbound states. For evaluation of ligand binding energies described below, MD simulations of the inhibitor unbound states (IUSs) were needed. Simulation systems of IUSs of the wild-type proteins and the V82T/I84V mutant were obtained by removing the inhibitor molecule from the structures of the inhibitor bound states (IBSs), respectively. The two carboxyl groups of Asp25 in the dimer were set to be both deprotonated based on experimental evidences [3,31]. For comparison, MD simulations for IUSs with the mono-protonated carboxyl groups of Asp25 and the deprotonated ones were also carried out. The procedure of the MD simulations of IUSs are the same as that of IBSs, and equilibrium MD simulations for 1 μs each for the three protonation states were performed.

Change in binding affinity of Indinavir upon the V82T/I84V mutation. Change in free

energy difference between IBS and IUS upon the mutation, $\Delta_{\text{M-WT}}\Delta_{\text{b}}F$, was evaluated through

a thermodynamic cycle (Figure 4),

$$\Delta_{\text{M-WT}}\Delta_{\text{b}}F \equiv \Delta_{\text{b}}F_{\text{M}} - \Delta_{\text{b}}F_{\text{WT}} = \Delta_{\text{M-WT}}F_{\text{IBS}} - \Delta_{\text{M-WT}}F_{\text{IUS}} \qquad (2)$$

where $\Delta_{\text{b}}F_{\text{M}}$ and $\Delta_{\text{b}}F_{\text{WT}}$ are free energy differences between IBS and IUS, i.e., binding

affinities, of the mutant and the wild-type protein, respectively. However, the direct simulations

of the ligand binding processes involving large conformational changes of the proteins and the

ligand molecules require considerably long MD calculations, and thus are computationally too

demanding. The evaluation of $\Delta_{\text{M-WT}}\Delta_{\text{b}}F$ is therefore converted into the calculations of free

energy differences between the mutant and the wild-type protein in IBS and IUS, $\Delta_{\text{M-WT}}F_{\text{IBS}}$

and $\Delta_{\text{M-WT}}F_{\text{IUS}}$, respectively, which were computed with alchemical FEP techniques [54,67-74].

In the case of $\Delta_{\text{M-WT}}F_{\text{IBS}}$ for the QM/MM systems, QM/MM contributions are also included

as

$$\Delta_{\text{M-WT}}F_{\text{IBS}} = \Delta_{\text{M-WT(QM)}}E_{\text{QM}} + \Delta_{\text{M-WT(QM)}}F_{\text{QM-MM,MM}} + \Delta_{\text{M-WT}}F_{\text{alchemy}} \qquad (3)$$

$\Delta_{\text{M-WT(QM)}}E_{\text{QM}}$ and $\Delta_{\text{M-WT(QM)}}F_{\text{QM-MM,MM}}$ are contributions of the QM energy, and the QM-MM

interaction energy and the MM one, respectively, upon change of the QM region from the wild-

type protein to the mutant while the mutation groups were unchanged. Those terms were first

computed by the FEP procedures described above where the geometry and the effective atomic

charges of the QM region were gradually altered from those of the wild-type protein to the mutant.

The geometry and the effective atomic charges of the QM parts were divided into 10 discrete points. The total length of the MD trajectory calculation was therefore 100 ns.

$\Delta_{\text{M-WT}} F_{\text{alchemy}}$ was then computed by the alchemical FEP calculation for the system including the fixed QM region of the mutant where the mutation groups were gradually changed with the dual-topology mode implemented in AMBER18 program package [77,78]. The parameters of atoms in the mutated residues were divided into 20 discrete states. The total length of the MD trajectory calculation is 200 ns. For comparison, the alchemical FEP calculations for IBS were performed by MD simulations where the QM region was treated with the MM force field. The free energy change upon the mutation for IUS, $\Delta_{\text{M-WT}} F_{\text{IUS}}$, was also evaluated by the alchemical FEP calculations with the same procedure.

The direction of the changes from the wild-type protein to the mutant is defined as the forward direction. The calculation in the backward direction from the mutant to the wild-type protein was also carried out to assess the statistical convergence. Note that the thermodynamic path in the backward direction does not coincide with that in the forward one. The FEP change in the forward direction is wild-type QM/wild-type MM → mutant QM/wild-type MM → mutant QM/mutant MM, and that in the backward one is mutant QM/mutant MM → wild-type QM/mutant MM → wild-type QM/wild-type MM. Thus, the intermediate states (mutant QM/wild-type MM vs. wild-type QM/mutant MM) in the thermodynamic paths are different.

RESULTS

We first compared structures of the Indinavir binding site of the wild-type protein and the V82T/I84V mutant obtained by MD simulations with classical MM force fields and the QM/MM RWFE-SCF free energy optimizations. Next, the protonation states of the two catalytic aspartic acids, Asp25(A) and Asp25(B), were determined by free energy calculations for the free energetically optimized structures obtained by the QM/MM RWFE-SCF method. Finally, change in the binding free energy of Indinavir upon the V82T/I84V mutation was evaluated with alchemical free energy perturbation calculations.

MD simulations of the wild-type protein and the V82T/I84V mutant. We performed MD simulations with classical MM force fields for 1 μs for the wild-type protein and the V82T/I84V mutant in the two mono-protonated states, AH and BH, where one of the catalytic aspartic acids, Asp25(A) and Asp25(B), is protonated, respectively (see COMPUTATIONAL METHODS). The two aspartic acids of Asp25 were experimentally suggested to be mono-protonated for asymmetric inhibitors [31-35]. Conformations of the sidechains of the protonated Asp25(A) and Asp25(B) of the wild-type protein observed in the MD simulations are distinctly different (Figures S4a-d) and not in C_2 symmetry because of the asymmetric binding of Indinavir despite the C_2 symmetry of the protein. The sidechain of the protonated Asp25(A) is also somewhat flexible, as suggested by a previous MD study [49], compared to that of the protonated Asp25(B) (Figure S4a,b). During

20

the MD simulations for 1 µs, water molecules move in and out of the binding site (Figures S5 and

S6). No significant structural differences of Asp25 and the water occupation between the wild-

type protein and the V82T/I84V mutant were found (Figures S4, S5, and S6). Details of the results

are described in Supporting Information.

QM/MM RWFE-SCF geometry optimizations. Structures of the bound Indinavir and the

catalytic Asp25 in the wild-type protein were refined by QM/MM RWFE-SCF geometry

optimizations starting from snapshots of the main conformations in the MD trajectories described

above (see COMPUTATIONAL METHODS for details). The free energetically optimized

structures of the wild-type protein (Figure 5a,b) showed that large conformational changes of

Asp25 are associated with occupations of more water molecules in the binding sites.

Prominent conformational changes appear at the deprotonated aspartic acids of Asp25. In the

initial conformations of the AH protonation state taken from the MD simulations, one of the two

O_δ atoms of the carboxyl group of Asp25(B) was hydrogen-bonded with two N-H groups of the

main chain amides of Gly27 of the protein dimer (Figure 6a). During the optimization, the

hydrogen-bond of the O_δ atom with one of the two N-H groups of Gly27 was dissociated, while

that with the other N-H group was maintained (Figure 6a). Orientation of the carboxyl group of

Asp25(B) was also significantly changed (Figures S7a,c,e and S8, and Table S2). The

conformational change of the deprotonated Asp25(B) was accompanied by hydration with water

molecules coming into cavities newly created by the conformational change, and consequently

four water molecules occupied the cavities in the binding pocket (Figures 5a and 7a). The water

hydration in the binding pocket was not observed in the X-ray crystallographic structure [12]. The

discrepancy may arise from the environment around the protein; the X-ray crystallographic

structure was determined in a crystal packing at high concentration of the protein, i.e., in much

fewer water molecules, while the protein is fully solvated in a water box in the present simulation

system. Given that no apparent counter ion group of the deprotonated Asp25 is found and the

hydration in the binding pocket is closely related to the protease function, i.e., hydrolysis of a

peptide bond, the hydration in the binding pocket observed in the present study seems physically

and biochemically reasonable.

Similar conformational changes of the deprotonated Asp25(A) and hydration with water

molecules during the QM/MM RWFE-SCF geometry optimization were also observed for the BH

protonation state (Figures 5b, 6b, 7b, and S7b,d,f). However, because of the asymmetric binding

of Indinavir, the conformational changes of the deprotonated Asp25(A) were less pronounced

(Figures 6b and S7b,d,f). Furthermore, although water molecules hydrating the catalytic aspartic

acids increased during the free energy optimization, cavities were not fully created around

Asp25(A) because of tight hydrophobic packing among the tertiary butyl and phenyl groups of

Indinavir and Val82 and Ile84 of the protein, and thus the deprotonated Asp25(A) was less

hydrated (Figure 7b). In addition, Asp25(B) was also less hydrated because Asp25(B) is protonated. Consequently, the number of water molecules occupying the cavities in the binding pocket in the BH state in the optimized structure was three (Figure 5b and 7b), which is less than that in the AH state, four, as described above (Figure 5a and 7a).

In addition to the conformational changes of the catalytic Asp25, molecular structures of Indinavir were also altered by the QM/MM free energy optimizations. Because of strong hydrogen-bonds of the hydroxy group of Indinavir with the carboxyl groups of Asp25, the conformational changes of Asp25 described above were correlated with a deeper binding of the hydroxy group of Indinavir inside the binding cleft (Figure 5e,f). The deeper binding of the hydroxy moiety of Indinavir was also achieved by rotations of dihedral angles of Indinavir's backbone bonds adjacent to the hydroxyl group (Table S3). The dihedral angles of N_3-C_{10}-C_{11}-C_{12} and C_{10}-C_{11}-C_{12}-C_{13} of the optimized structure in the AH state deviated remarkably from those in the X-ray crystallographic structure by 17.1 and -22.4 degrees, respectively, and in the MD simulation with the MM force fields by 26.5 and -11.1 degrees, respectively. Several dihedral angles around N_3-C_{10}, C_{11}-C_{12}, and C_{13}-C_{21} determined by the QM/MM RWFE-SCF optimizations were also found to deviate by more than 10 degrees from those of the MD simulations with the MM force field. Those dihedral angles are influenced by the deeper binding of Indinavir described above, as they are located in the vicinity of the hydroxy group hydrogen-bonded with Asp25.

Internal molecular structures of other moieties of Indinavir were also changed by the QM/MM free energy optimizations (Table S3). The dihedral angles around C_{31}-C_{32} in the QM/MM optimized structure changed largely from those in the MD simulation with the MM force field by ~20 degrees. The dihedral angles represent rotation of the pyridyl group which involves complex change of hyperconjugation (σ-π interaction) between the σ orbital of N_1-C_{31} and the π orbitals of the pyridyl ring and thus is difficult to describe with the MM force field. The high accuracy of the QM description improved the interaction and thus successfully refined the molecular structure. The difference in the conformation of the pyridyl group of Indinavir may also be correlated with hydrophobic interaction of the group with Pro81(B) and Val82(B) of the protein (Figure 8). The hydrophobic sidechains of Pro81(B) and Val82(B) formed a more compact conformation with the aromatic pyridyl group (Figure 8b) in the QM/MM samples, while a looser conformation of those sidechains (Figure 8c) was frequently found in the MM samples, implying that a stronger hydrophobic interaction of the pyridyl group of Indinavir is established in the QM/MM optimized structure.

The dihedral angles around C_{31}-C_{32} in the QM/MM optimized structure also largely deviated by ~37 degrees from that in the X-ray crystallographic structure (Figure 5e,f and Table S3). The deviation is attributed to difference in environment around the pyridyl group between the X-ray crystallographic structure and the simulation system. The pyridyl group is exposed to bulk water

environment in the simulation system and thus its environment is expected to be very different

from the environment of the X-ray crystallographic structure influenced by crystal packing. The

dihedral angles of C_{22}-C_{23} and C_{23}-C_{24} optimized by the QM/MM RWFE-SCF calculations also

deviated from those obtained by the MD simulations with the MM force field, indicating that the

ab initio description improved the conformation around those dihedral angles.

The structures of Indinavir and its binding site in the V82T/I84V mutant were also refined by

equilibrium MD simulations for 500 ns each and the following QM/MM RWFE-SCF geometry

optimizations from starting structures obtained based on the QM/MM optimized structures of the

wild-type proteins described above (see COMPUTATIONAL METHODS). In the case of the AH

state, the conformations of Asp25, the water hydration around them, and the internal structure of

Indinavir for the V82T/I84V mutant were almost the same as those for the wild-type protein

(Figures 5a,c, 7c, S9a, and S10a).

In the case of the BH state, because a cavity around Asp25(B) is enlarged by the I84V mutation

where the size of the sidechain at the position of 84 decreases, one water molecule around

Asp25(B), which was excluded from the binding site upon formation of the BH state from the AH

one for the wild-type protein as described above (Figure 5a,b), partially occupied the cavity in the

BH state in an equilibrium MD simulation for 500 ns before the QM/MM optimization (Figure

S9b). The occupation of the additional one water molecule may also be reinforced by increase of

polarity by the V82T mutation. Consequently, the number of the hydrating water molecule in the

binding pocket in the BH state of the V82T/I84V mutant fluctuates between three and four and

increased from that of the wild-type protein (Figures 7d and S9b).

Because of the increased hydration of Asp25(B) for the V82T/I84V mutant, the proton attached

to Asp25(B) spontaneously transferred to Asp25(A) through the hydroxy group of Indinavir in an

early cycle of the following QM/MM RWFE-SCF geometry optimization around 50 ns, leading

to formation of the AH state. The spontaneous proton translocation forming the AH state clearly

indicates that a free-energetically quasi-stable state does not exist for the V82T/I84V mutant in

the BH state, and thus the protonation state of the V82T/I84V mutant is the AH one.

For the free energy calculations of the protonation states described later, a model of the

V82T/I84V mutant in the BH state was obtained by the QM/MM RWFE-SCF geometry

optimization with a fixed distance of the O-H group of Asp25(B) which prevents the spontaneous

proton transfer forming the AH state (see COMPUTATIONAL METHODS). The conformation

of Asp25 and the internal structure of Indinavir were again almost the same as those of the wild-

type protein in the BH state (Figures 5b,d and S10b). The number of the water molecules

hydrating Asp25 in the binding sites in the BH state increased to nearly four as described above,

which is the same as that in the AH state (Figures 5c,d and 7c,d)

The protein structure of the binding site with Indinavir does not exhibit significant change upon

26

the V82T/I84V mutations (Figure 9). RMFSs of the amino acids in the binding sites, their

differences between the wildtype and the V82T/I84V mutant, and the averaged C_α-distances

between them were small in IBS in the AH state. Nevertheless, the largest RMSFs and C_α-

distances appear in the region from Pro81(B) to Ile84Val(B), indicating that the hydrophobic

packing of this region of the protein with Indinavir seen above (Figure 8) was somewhat perturbed

by the mutations. Unlike in IBS, RMSFs of the binding site in IUS are relatively large because

the amino acids in the binding site is exposed to bulk water in IUS.

Finally, one water molecule tetrahedrally bridging two amide oxygen atoms of Indinavir (O_1

and O_3 atoms) and two amide nitrogen atoms of Ile50(A) and Ile50(B) through hydrogen-bonds

was found for all of the optimized structures, respectively (Figure S11). The bridging structural

water molecule was observed by various experiments including the X-ray crystallographic

structure (1HSG) employed in the present study [1,4,5,12], and is considered to strengthen the

binding of Indinavir.

Protonation states of the catalytic aspartic acids of Asp25. Free energy differences between

the AH state and the BH one, optimized by the QM/MM RWFE-SCF methods described above

were evaluated by MD simulations of FEP calculations with BAR method (see

COMPUTATIONAL METHODS). The free energy difference, $\Delta_{\text{BH-AH}}F_{\text{QM/MM}}$, was computed to

be 2.8 kcal/mol (Table 1), indicating that the AH state is energetically more stable than the BH

one. Ample sampling of the long MD simulations in the forward and backward directions for 1

μs each provided a sufficient statistical convergence represented by small difference between

$\Delta_{\text{BH-AH}}F_{\text{QM/MM}}$ obtained in those directions by 0.4 kcal/mol, while shorter MD simulations led to

larger deviations of $\Delta_{\text{BH-AH}}F_{\text{QM/MM}}$ by several kcal/mol (Tables 1 and S4). Dependency of density

functional used in the QM/MM calculation on the free energy difference was also assessed by

computing $\Delta_{\text{BH-AH}}E_{\text{QM}}$ in Eq. (1) with various density functionals at the same optimized QM

geometry and the same mean field of electrostatic potential from the MM region. Deviations from

the value with B3LYP-D3 functional employed in the present study were less than 1.5 kcal/mol

(Tables S5), and thus the conclusion that the AH state is energetically more stable holds.

The free energy difference originates from two contributions of the QM energy, $\Delta_{\text{BH-AH}}E_{\text{QM}}$,

and the QM-MM interaction energy and the MM energy, $\Delta_{\text{BH-AH}}F_{\text{QM-MM,MM}}$, respectively, as

shown in Eq. (1). $\Delta_{\text{BH-AH}}E_{\text{QM}}$ gave a largely negative contribution of -18.1 kcal/mol, indicating

that the QM energy in the BH state is considerably lower than that in the AH state. Given that the

QM region includes Indinavir and the catalytic carboxylic acids of Asp25, and the internal

conformations of Indinavir in the AH and BH states are not significantly different, the large energy

QM contribution is attributed to the difference in the interaction of Indinavir with Asp25 due to

the asymmetric binding. The hydroxy group of Indinavir therefore energetically favors interaction

with the deprotonated Asp25(A) in the BH state over the deprotonated Asp25(B) in the AH state,

as the hydroxy group interacts more strongly with the anionic deprotonated carboxylic acid than the neutral protonated one.

In contrast, the other contribution of $\Delta_{\text{BH-AH}}F_{\text{QM-MM,MM}}$, 20.9 kcal/mol, was largely positive, and overcompensated that of $\Delta_{\text{BH-AH}}E_{\text{QM}}$, leading to the small positive overall contribution of $\Delta_{\text{BH-AH}}F_{\text{QM/MM}}$, 2.8 kcal/mol. The large positive contribution of $\Delta_{\text{BH-AH}}F_{\text{QM-MM,MM}}$ comes from the asymmetric hydration of the catalytic carboxylic acids, Asp25, as described above (Figure 5a,b). As Asp25(B) is more hydrated than Asp25(A), the AH state where Asp25(B) is deprotonated and negatively charged, is more stabilized than the BH one.

The protonation state of the V82T/I84V mutant was determined to be the AH state by the QM/MM RWFE-SCF optimization where the proton at Asp25(B) in the BH state was spontaneously transferred to Asp25(A) as described above. The protonation state of the mutant was also verified in terms of energetics by the FEP calculations. The BH state was modeled by the QM/MM RWFE-SCF optimization with a fixed O-H bond length of the protonated Asp25(B) as described above. The free energy difference, $\Delta_{\text{BH-AH}}F_{\text{QM/MM}}$, was evaluated to be 4.6 kcal/mol (Table 1), and thus the AH state is energetically more stable than the BH state, which agrees with the observation of the QM/MM RWFE-SCF optimization described above. Furthermore, the free energy difference of the mutant is larger by 1.6 kcal/mol than that of the wild-type protein, which is in line with the spontaneous proton transfer during the QM/MM RWFE-SCF optimization.

As in the case of the wild-type protein, $\Delta_{BH\text{-}AH}E_{QM}$ of the mutant, -13.2 kcal/mol, was largely negative and the largely positive contribution of $\Delta_{BH\text{-}AH}F_{QM\text{-}MM,MM}$, 17.8 kcal/mol, overcompensated $\Delta_{BH\text{-}AH}E_{QM}$, resulting in the positive overall free energy difference, $\Delta_{BH\text{-}AH}F_{QM/MM}$ (Table 1). However, $\Delta_{BH\text{-}AH}E_{QM}$ of the mutant is significantly larger by 4.9 kcal/mol than that of the wild-type protein, which leads to the larger $\Delta_{BH\text{-}AH}F_{QM/MM}$ of the mutant. Given that the conformations of the binding site of the wild-type protein and the mutant in the AH state are similar, and thus the AH states are not likely responsible for the change, the increase of $\Delta_{BH\text{-}AH}E_{QM}$ of the mutant is attributed to the stronger hydration of the protonated Asp25(B) in the BH state (Figure 5b,d). As described above, the number of the water molecules hydrating the protonated Asp25(B) in the mutant is larger than that in the wild-type protein. The stronger hydration of the protonated Asp25(B) which decreases its pKa elevates more largely the QM energy of the BH state.

Effect of the V82T/I84V drug-resistant mutation on binding affinity of Indinavir. We first refined the QM/MM structures and the energies by QM/MM RWFE-SCF free energy optimizations with DFT M06-2X functional [88] from those obtained with DFT B3LYP-D3 functional (see COMPUTATIONAL METHODS). In an ongoing computational study on enzymatic catalysis of HIV-1 protease in our group, we found that a free energy of an active reaction intermediate is strongly dependent on density functionals employed, and that obtained

30

with M06-2X functional is in better agreement with that at a higher level of theory, which will be

reported elsewhere. As the binding free energies of the inhibitor molecule evaluated in the present

study will be compared with those of the transition states of the enzymatic reactions to elucidate

molecular mechanism of the drug resistance as described above, we obtained the formers with the

same M06-2X functional as well. The optimized structures of the wild-type proteins and the

V82T/I84V mutant with M06-2X functional were found to undergo very minor changes from

those obtained with B3LYP-D3 functional (Figure S12). The RMSDs of the heavy atoms of the

QM regions optimized with M06-2X functional with respect to those with B3LYP-D3 one are

0.10 Å and 0.14 Å for the wild-type protein and the V82T/I84V mutant, respectively. The compact

packing of the pyridyl group of Indinavir and Pro81(B) and Val82(B) of the protein observed in

the optimized structure with B3LYP-D3 functional was maintained as well in the M06-2X

structure (Figure S13).

Free energy calculations of the difference in the binding free energy between the wild-type

protein and the mutant, $\Delta_{\text{M-WT}}\Delta_{\text{b}}F$, based on Eqs. (2) and (3) showed that the binding free

energy of Indinavir increased by 3.8 kcal/mol upon the mutation of V82T/I84V (Table 2),

indicating that the mutation significantly reduces the binding affinity of Indinavir. Deviation of

the free energy differences obtained by the FEP calculations in the forward direction and the

backward one was small (0.2 kcal/mol) despite that their thermodynamic paths did not coincide

as described above, showing a sufficient statistical convergence. The computed increase of the

binding free energy is in line with the experimental observations, i.e. increase of the binding free

energy by 2.5-3.0 kcal/mol [13,14], although the computed value is slightly overestimated.

As shown in Eq. (2), $\Delta_{\text{M-WT}}\Delta_b F$ is given by a difference between free energy changes of the

inhibitor binding state (IBS) and the inhibitor unbinding state (IUS) upon the mutation,

$\Delta_{\text{M-WT}}F_{\text{IBS}}$ and $\Delta_{\text{M-WT}}F_{\text{IUS}}$, respectively. Furthermore, the former is composed of contributions

of the QM energy, $\Delta_{\text{M-WT(QM)}}E_{\text{QM}}$, the QM-MM interaction energy and the MM energy,

$\Delta_{\text{M-WT(QM)}}F_{\text{QM-MM,MM}}$, and the alchemical mutation, $\Delta_{\text{M-WT}}F_{\text{alchemy}}$, as shown in Eq. (3).

$\Delta_{\text{M-WT(QM)}}E_{\text{QM}}$ and $\Delta_{\text{M-WT(QM)}}F_{\text{QM-MM,MM}}$ represent the contributions of conformational

changes of the QM region. The contribution of $\Delta_{\text{M-WT(QM)}}E_{\text{QM}}$ gave an increase of 1.7 kcal/mol,

and was almost compensated by that of $\Delta_{\text{M-WT(QM)}}F_{\text{QM-MM,MM}}$, -1.6 kcal/mol. The contribution of

the alchemical mutation between IBS and IUS, $\Delta_{\text{M-WT}}F_{\text{alchemy}} - \Delta_{\text{M-WT}}F_{\text{IUS}}$, then added an

increase of 3.7 kcal/mol, and consequently the V82T/I84V mutation increased the overall free

energy difference, $\Delta_{\text{M-WT}}\Delta_b F$, by 3.8 kcal/mol.

The increase of $\Delta_{\text{M-WT}}\Delta_b F$ is considered to originate from reduction of hydrophobic

interaction of Indinavir with the V82T/I84V mutant. It is noteworthy that $\Delta_{\text{M-WT}}\Delta_b F$ evaluated

with the MD simulations with the MM force field of Indinavir was small, 0.3 kcal/mol (Table 2).

As described above (Figures 8 and S13), the pyridyl group of Indinavir established a strong

hydrophobic interaction with Val82(B) in the QM/MM samples, while the hydrophobic structure

was looser in the MM samples. The observation is therefore consistent with the increase of

$\Delta_{\text{M-WT}}\Delta_b F$ by the QM/MM calculation as the hydrophobic interaction becomes weaker in the

V82T/I84V mutant where a polar hydroxyl group is introduced at the position 82 and the bulky

hydrophobic group at the position 84 is replaced with the smaller one.

Equilibrium MD simulations of IUS for 1 μs showed large conformational fluctuation of the

flap region (Figure S14), although no distinct conformational transitions to the open or semi-open

conformations observed by an X-ray crystallographic measurement and previous MD simulations

[56,92-94] were found during the simulation time, which may be a source of the slight

overestimation of the increase of $\Delta_{\text{M-WT}}\Delta_b F$. We also performed the alchemical FEP

calculations for IUS with different protonation states of the carboxylic acids of Asp25, i.e., the

mono-protonated state and the di-protonated state, for comparison, and found that the difference

in the protonation state moderately altered the free energy change upon the mutation by ~1

kcal/mol (Table S6).

DISCUSSION AND CONCLUDING REMARKS

The present molecular simulations with the QM/MM free energy optimization and alchemical free energy calculation techniques successfully reproduced the significant reduction of binding affinity of an inhibitor, Indinavir, due to a drug resistant mutation, V82T/I84V, and elucidated the molecular mechanism underlying the affinity change. The complex molecular structures of Indinavir bound in the protein were accurately determined at the density functional level of electronic structure theory on extensive free energy surfaces of the protein represented by the long-time MD simulations on microseconds timescale. The accurate description of the molecular structures of Indinavir successfully identified the molecular origin of the reduction of the binding affinity upon the mutation.

The reduction of the binding affinity upon the mutation was, however, not well reproduced by the calculations only with MM force fields for the Indinavir binding. In fact, significant differences in the internal molecular geometry of Indinavir and its interaction with the protein between the QM/MM free energetically optimized structure and the MM force field one were observed. Especially, the position of Indinavir where the significant geometric difference appeared due to complex electronic interaction of hyperconjugation close to the protein residues related to the V82T/I84V mutation. It is therefore suggested that the accurate description of the present approach is necessary for properly capturing the impact of the subtle structural changes

due to the drug-resistant mutation. As the present approach allows one to avoid difficulties in

accurately developing MM energy functions of complex ligand molecules, the approach is

capable of accurately and consistently evaluating relative binding affinities of various inhibitor

molecules and drug-resistant mutants required for in silico drug design.

The QM/MM approach always needs to set the QM and MM regions properly to diminish

errors originating from lack of electronic interactions between the QM and MM regions and

within the MM one such as electronic polarization and charge transfer [95-99]. In the present

study, Indinavir and the sidechains of the catalytic Asp25 were included in the QM region. As

described above, the QM treatment of the former succeeded in accurately describe its

conformation, and the strong electronic interaction between Indinavir and the charged aspartate

was taken into account by including the catalytic Asp25 in the QM region.

Other than Asp25, however, the amino acids of the binding site contacting Indinavir are mainly

hydrophobic. The interaction of the Indinavir with those hydrophobic amino acids are thus

considered to be reasonably described by the MM interaction which was utilized for the

interaction at the QM-MM boundary in the present calculation as hydrophobic interaction does

not involve large change of the electronic wavefunction. Furthermore, because thermally driven

conformational changes are essential for proper description of hydrophobic interaction, the long-

time MD sampling of the hydrophobic group of the binding site in the MM region in the present

QM/MM RWFE-SCF calculations successfully captured significant changes in the hydrophobic interaction of Pro81(B) and Val82Thr(B) upon the V82T/I84V mutations likely leading to the binding free energy reduction as described above. It is therefore considered that the QM/MM partition of the present study provided a well-balanced description of the ligand binding interaction in terms of accuracy and computational costs.

X-ray crystallographic studies reported conformational changes of the protein upon mutations [13,15,20,23]. X-ray crystallographic structures of HIV-1 protease binding Indinavir exhibit large conformational changes of 80s loop comprised of amino acids 79-83 and the pyridyl group of Indinavir upon nine mutations including V82T [20] and two mutations including V82A [23], while significant conformational changes upon four mutations including V82T/I84V were absent in an X-ray crystallographic structure [13]. The experimental observations that the mutations at the position of 82 induce conformational changes of 80s loop are therefore in line with the present calculations showing that the hydrophobic interaction of the pyridyl group of Indinavir with the amino acids at the positions of 81 and 82 in 80s loop are responsible for changing the binding free energy upon the V82T/I84V mutation. However, the different behavior of the conformational changes of 80s loop upon the mutations in the X-ray crystallographic structure described above may imply that the conformational changes are affected by crystal packing as the loop is flexible and is located on the protein surface. The significant role of the pyridyl group of Indinavir in the

binding is also consistent with an experimental evidence that modification of the pyridyl group

of Indinavir to more hydrophobic methylenedioxyphenyl group increased binding affinity of triple

a mutant including V82T/I84V [15], and a previous MD simulation for 1 ns showing disorder of

the pyridyl group in the V82A mutant [52].

Although the present calculations semi-quantitatively reproduced the reduction of the binding

affinity upon the drug-resistant mutation, however, the increase of the free energy difference was

slightly overestimated by ~1 kcal/mol. Two possible sources of the error are considered. First, the

protein conformation in the inhibitor unbound state might not be well modeled as described above.

It is, however, noteworthy that when the binding free energy change upon mutations for the

inhibitor molecule is compared to that for the wild-type substrate in the catalytic process, through

which the ability of the mutations for drug-resistance is evaluated as described above, the ligand

unbound state does not appear in the thermodynamic cycle for the free energy comparison. Second,

the present QM/MM free energy optimization technique neglects conformational fluctuation of

the QM region, which may overestimate stability of the hydrophobic packing. The error is

considered to be relatively minor in the present case of the Indinavir binding as tight binding of

the inhibitor molecule in the protein was observed. However, for an inhibitor molecule with

flexible groups, the lack of conformational fluctuation of the QM region may cause a problem in

accurately evaluating the free energies. A correction scheme to take conformational fluctuation of

the QM region into account needs to be developed in the future study.

The protonation state of the sequentially symmetric catalytic carboxyl groups, Asp25(A) and Asp25(B), was also determined by direct calculations of free energy differences between the protonation states. The consistent combination of the high accuracy of the density functional theories for the QM description and the ample conformational samples obtained by the long-time MD simulations for microseconds for the MM protein environments thoroughly determined the protonation states, and the underlying mechanism based on the highly accurate and statistically well-converged free energy differences was clarified. Especially, the small overall free energy differences between the protonation states (3-5 kcal/mol) were given by sums of large positive and negative contributions of the electronic energies and the interactions with the protein and hydrating water molecules, respectively (Table 1), created by the asymmetrically bound ligand. The high accuracies of both the electronic state of the titratable groups and their interaction with the statistically reorganizing surroundings responding to large changes of electrostatic environment due to the protonation change were therefore important for the determination of the protonation state.

The protonation state of the catalytic Asp25 were widely investigated by theoretical studies through various approaches such as potential energy calculations with MM force field, semiempirical and ab initio QM calculations, and free energy calculations with an MM Poisson-

Boltzmann Surface Area method with MD simulations for several nanoseconds [37,38,41,42,45].

The present calculation which combined highly accurate methods of the ab initio QM description

and the long-time microscopic MD simulation on sub-micro to micro second time scale showed

that the hydration of water molecules to the aspartates and the (de)protonation electronic energy

of them are correlated in a complex manner, and both significantly contribute to the energetics of

the protonation state. Because descriptions of the former and latter processes require a long-time

MD simulation and an accurate ab initio QM description, respectively, a careful treatment is

necessary to determine the protonation state theoretically.

To understand molecular mechanism of the drug-resistance, the impacts of the mutations on

both of the enzymatic activity and the inhibitor binding need to be examined as described above.

The enzymatic catalytic activity, k_{cat}/K_m, is measured by the free energy difference between the

substrate unbound state and the transition state of the enzymatic reaction. Thus, in the case of

examining effect of a mutation on the catalytic activity, the free energy difference between the

transition states in the wild-type protein and the mutant is calculated, and explicit evaluation of

the binding free energies of the substrate can be omitted similar to the present study (Figure 4).

The theoretical investigation on the enzymatic chemical reaction inevitably requires accurate

quantum chemical treatment. The present study demonstrated that the inhibitor binding process

can be examined quantitatively by the accurate QM/MM free energy optimization approach that

is directly applicable to the catalytic reaction process as well [57-59], and therefore opens the way for understanding the molecular mechanism of drug-resistance through direct quantitative comparison of those processes with the same accuracy, which is now ongoing in our group and will be reported elsewhere.

DATA AND SOFTWARE AVAILABILITY

Coordinate data of the free energetically optimized structures of the QM region for all the states

obtained in the present study are included in Supporting Information. See COMPUTATIONAL

METHODS and Supporting Information for detailed descriptions of softwares along with

workflows and parameter setting of the simulations. The locally developed codes for the QM/MM

RWFE-SCF calculation used in the present study are available upon request.

ASSOCIATED CONTENT

The Supporting Information is available.

Supplemental computational methods, supplemental results of classical MD simulations, an amino acid sequence of the HIV-1 protease used in this study (Figure S1), summary of predicted protonation state of Asp25 in previous studies (Table S1), comparison of amino acid sequences between two HIV-1 proteases (Figure S2), protein environments around Indinavir and a natural substrate (Figure S3), results of MD simulations with classical MD simulations (Figures S4-S6, S14), analysis of hydrogen bonding network of Indinavir binding region (Figures S7-S8, Table S2), analysis of internal dihedral angles of Indinavir (Table S3), number of water molecules around Indinavir binding region during MD simulations before free energy optimizations of V82T/I84V mutant (Figures S9), results of QM/MM free energy optimizations (Figures S10-S13), evaluation of $\Delta_{\text{BH-AH}}F_{\text{QM-MM,MM}}$ by BAR method of FEP for various lengths of MD trajectories (Table S4), evaluation of $\Delta_{\text{BH-AH}}E_{\text{QM}}$ for various DFT functionals (Table S5), alchemical free energy evaluation of IUS for difference protonation states of Asp25 (Table S6), and description for coordinate data in zip archive file (PDF).

One zip archive file of coordinate data of the free-energetically optimized geometries of the QM region by the QM/MM RWFE-SCF calculations for all the states obtained in this study (ZIP).

ACKNOWLEGEMENT

REFERENCES

(1) Ali, A.; Bandaranayake, R. M.; Cai, Y.; King, N. M.; Kolli, M.; Mittal, S.; Murzycki, J. F.; Nalam, M. N. L.; Nalivaika, E. A.; Özen, A.; Prabu-Jeyabalan, M. M.; Thayer, K.; Schiffer, C. A. Molecular Basis for Drug Resistance in HIV-1 Protease. *Viruses* **2010**, *2*, 2509-2535.

(2) Wensing, A. M. J.; van Maarseveen, N. M.; Nijhuis, M. Fifteen years of HIV Protease Inhibitors: raising the barrier to resistance. *Antivir. Res.* **2010**, *85*, 59-74.

(3) Ido, E; Han, H.; Kezdy, F. J.; Tang, J. Kinetic Studies of Human Immunodeficiency Virus Type 1 Protease and Its Active-site Hydrogen Bond Mutant A28S. *J. Bio. Chem.* **1991**, *266*, 24359-24366.

(4) Prabu-Jeyabalan, M.; Nalivaika, E.; Schiffer, C. A. How Does a Symmetric Dimer Recognize an Asymmetric Substrate? A Substrate Complex of HIV-1 Protease. *J. Mol. Biol.* **2000**, *301*, 1207-1220.

(5) Baldwin, E. T.; Bhat, T. N.; Gulnik, S.; Liu, B.; Topol, I. A.; Kiso, Y.; Mimoto, T.; Mitsuya, H.; Erickson, J. W. Structure of HIV-1 protease with KNI-272, a tight-binding transition-state analog containing allophenylnorstatine. *Structure* **1995**, *3*, 581-590.

(6) Brik, A.; Wong, C.-H. HIV-1 protease: mechanism and drug discovery. *Org. Biomol. Chem.* **2003**, *1*, 5-14.

(7) Trova, M. P.; Babine, R. E.; Byrn, R. A.; Casscles, Jr., W. T.; Hastings, R. C. Synthesis and

biological evaluation of a series of HIV-1 protease inhibitors. *Bioorg. Med. Chem. Lett.* **1993**, *3*, 1595-1600.

(8) Askin, D.; Eng, K. K.; Rossen, K.; Purick, R. M.; Wells, K. M.; Volante, R. P.; Reider, P. J. Highly Diastereoselective Reaction of a Chiral, Non-Racemic Amide Enolate with (*S*)-Glycidyl Tosylate. Synthesis of the Orally Active HIV-1 Protease Inhibitor L-735,524. *Tetrahedron Lett.* **1994**, *35*, 673-676.

(9) Vacca, J. P.; Dorsey, B. D.; Schleif, W. A.; Levin, R. B.; McDaniel, S. L.; Darke, P. L.; Zugay, J.; Quintero, J. C.; Blahy, O. M.; Roth, E.; Sardana, V. V.; Schlabach, A. J.; Graham, P. I.; Condra, J. H.; Gotlib, L.; Holloway, M. K.; Lin, J.; Chen, I-W.; Vastag, K.; Ostovic, D.; Anderson, P. S.; Emini, E. A.; Huff, J. R. L-735,524: An orally bioavailable human immunodeficiency virus type 1 protease inhibitor. *Proc. Natl. Acad. Sci. USA* **1994**, *91*, 4096-4100.

(10) Dorsey, B. D.; Levin, R. B.; McDaniel, S. L.; Vacca, J. P.; Guare, J. P.; Darke, P. L.; Zugay, J. A.; Emini, E. A.; Schleif, W. A.; Quintero, J. C.; Lin, J. H.; Chen, I-W.; Holloway, M. K.; Fitzgerald, P. M. D.; Axel, M. G.; Ostovic, D.; Anderson, P. S.; Huff, J. R. L-735,524: The Design of a Potent and Orally Bioavailable HIV Protease Inhibitor. *J. Med. Chem.* **1994**, *37*, 3443-3451.

(11) Dorsey, B. D.; McDaniel, S. L.; Levin, R. B.; Vacca, J. P.; Darke, P. L.; Zugay, J. A.; Emini, E. A.; Schleif, W. A.; Lin, J. H.; Chen, I-W.; Holloway, M. K.; Anderson, P. S.; Huff, J. R. Synthesis and evaluation of pyridyl analogs of L-735,524: Potent HIV-1 protease inhibitors.

Bioorg. Med. Chem. Lett. **1994**, *4*, 2769-2774.

(12) Chen, Z.; Li, Y.; Chen, E.; Hall, D. L.; Darke, P. L.; Culberson, C.; Shafer, J. A.; Kuo, L. C. Crystal Structure at 1.9-Å Resolution of Human Immunodeficiency Virus (HIV) II Protease Complexed with L-735,524, an orally Bioavailable Inhibitor of the HIV Proteases. *J. Biol. Chem.* **1994**, *269*, 26344-26348.

(13) Chen, Z.; Li, Y.; Schock, H. B.; Hall, D.; Chen, E.; Kuo, L. C. Three-dimensional Structure of a Mutant HIV-1 Protease Displaying Cross-resistance to All Protease Inhibitors in Clinical Trials. *J. Biol. Chem.* **1995**, *270*, 21433-21436.

(14) Shock, H. B.; Garsky, V. M.; Kuo, L. C. Mutational Anatomy of an HIV-1 Protease Variant Conferring Cross-resistance to Protease Inhibitors in Clinical Trials. *J. Biol. Chem.* **1996**, *271*, 31957-31963.

(15) King, N. M.; Melnick, L.; P.-Jeyabalan, M.; Nalivaika, E. A.; Yang, S.-Shong; Gao, Y.; Nie, X.; Zepp, C.; Heefner, D. L.; Schiffer, C. A. Lack of synergy for inhibitors targeting a multi-drug-resistant HIV-1 protease. *Protein Science* **2002**, *11*, 418-429.

(16) Maschera, B.; Darby, G.; Palú, G.; Wright, L. L.; Tisdale, M.; Myers, R.; Blair, E. D.; Furfine, E. S. Human Immunodeficiency Virus. Mutations in the viral protease that confer resistance to saquinavir increase the dissociation rate constant of the protease-saquinavir complex. *J. Biol. Chem.* **1996**, *271*, 33231-33235.

(17) Ridky, T. W.; Kikonyogo, A.; Leis, J. Drug-Resistant HIV-1 Proteases Identify Enzyme Residues Important for Substrate Selection and Catalytic Rate. *Biochemistry* **1998**, *37*, 13835-13845.

(18) Gulnik, S. V.; Suvorov, L. I.; Liu, B.; Yu, B.; Anderson, B.; Mitsuya, H.; Erickson, J. W. Kinetic Characterization and Cross-Resistance Patterns of HIV-1 Protease Mutants Selected under Drug Pressure. *Biochemistry* **1995**, *34*, 9282-9287.

(19) Partaledis, J. A.; Yamaguchi, K.; Tisdale, M.; Blair, E. E.; Falcione, C.; Maschera, B, Myers, R. E.; Pazhanisamy, S.; Futer, O.; Cullinan, A. B.; Stuver, C. M.; Byrn, R. A.; Livingston, D. J. In Vitro Selection and Characterization of Human Immunodeficiency Virus Type 1 (HIV-1) Isolates with Reduced Sensitivity to Hydroxyethylamino Sulfonamide Inhibitors of HIV-1 Aspartyl Protease. *J. Virol.* **1995**, *69*, 5228-5235.

(20) Munshi, S.; Chen, Z.; Yan, Y.; Li, Y.; Olsen, D. B.; Schock, H. B.; Galvin, B. B.; Dorsey, B.; Kuo, L. C. An alternate binding site for the P1-P3 group of a class of potent HIV-1 protease inhibitors as a result of concerted structural change in the 80s loop of the protease. *Acta Crystallogr. D Biol. Crystallogr.* **2000**, *56*, 381-388.

(21) Mahalingam, B.; Louis, J. M.; Hung, J.; Harrison, R. W.; Weber, I. T. Structural Implications of Drug-Resistant Mutants of HIV-1 Protease: High-Resolution Crystal Structures of the Mutant Protease/Substrate Analogue Complexes. *Proteins* **2001**, *43*, 455-464.

(22) Prabu-Jeyabalan, M.; Nalivaika, E. A.; King, N. M.; Schiffer, C. A. Viability of a Drug-Resistant Human Immunodeficiency Virus Type 1 Protease Variant: Structural Insights for Better Antiviral Therapy. *J. Virol.* **2003**, *77*, 1306-1315.

(23) Mahalingam, B.; Wang, Y.-F.; Boross, P. I.; Tozser, J.; Louis, J. M.; Harrison, R. W.; Weber, I. T. Crystal structures of HIV protease V82A and L90M mutants reveal changes in the indinavir-binding site. *Eur. J. Biochem.* **2004**, *271*, 1516-1524.

(24) Kovalevsky, A. Y.; Tie, Y.; Liu, F.; Boross, P. I.; Wang, Y-F.; Leshchenko, S.; Ghosh, A. K.; Harrison, R. W.; Weber, I. T. Effectiveness of Nonpeptide Clinical Inhibitor TMC-114 on HIV-1 Protease with Highly Drug Resistant Mutations D30N, I50V, and L90M. *J. Med. Chem.* **2006**, *49*, 1379-1387.

(25) Rhee, S-Y.; Taylor, J.; Fessel, W. J.; Kaufman, D.; Towner, W.; Troia, P.; Ruane, P.; Hellinger, J.; Shirvani, V.; Zolopa, A.; Shafer, R. W. HIV-1 Protease Mutations and Protease Inhibitor Cross-Resistance. *Antimicrob. Agents Chemother.* **2010**, *54*, 4253-4261.

(26) Agniswamy, J.; Louis, J. M.; Roche, J.; Harrison, R. W.; Weber, I. T. Structural Studies of a Rationally Selected Multi-Drug Resistant HIV-1 Protease Reveal Synergistic Effect of Distal Mutations on Flap Dynamics. *PLoS ONE* **2016**, *11*, e0168616-e0168633.

(27) Baxter, J. D.; Chasanov, W. M.; Adams, J. L. An Update on HIV-1 Protease Inhibitor Resistance. *J. AIDS Clin. Res.* **2016**, *7*, 581-587.

(28) Wensing, A. M.; Calvez, V.; Günthard, H. F.; Johnson, V. A.; Paredes, R.; Pillay, D.; Shafer, R. W.; Richman, D. D. 2017 Update of the Drug Resistance Mutations in HIV-1. *Top. Antivir. Med.* **2017**, *24*, 132-141.

(29) Hyland, L. J.; Tomaszek, Jr., T. A.; Meek, T. D. Human Immunodeficiency Virus-1 Protease. 2. Use of pH Rate Studies and Solvent Kinetic Isotope Effects To Elucidate Details of Chemical Mechanism. *Biochemistry* **1991**, *30*, 8454-8463.

(30) Yamazaki, T.; Nicholson, L. K.; Torchia, D. A.; Wingfield, P.; Stahl, S. J.; Kaufman, J. D.; Eyermann, C. J.; Hodge, C. N.; Lam, P. Y. S.; Ru, Y.; Jadhav, P. K.; Chang, C-H.; Weber, P. C. NMR and X-ray Evidence That the HIV Protease Catalytic Aspartyl Groups Are Protonated in the Complex Formed by the Protease and a Non-Peptide Cyclic Urea-Based Inhibitor. *J. Am. Chem. Soc.* **1994**, *116*, 10791-10782.

(31) Smith, R.; Brereton, I. M.; Chai, R. Y.; Kent, S. B. H. Ionization states of the catalytic residues in HIV-1 protease. *Nat. Struct. Biol.* **1996**, *3*, 946-950.

(32) Wang, Y-X.; Freedberg, D. I.; Yamazaki, T.; Wingfield, P. T.; Stahl, S. J.; Kaufman, J. D.; Kiso, Y.; Torchia, D. A. Solution NMR Evidence That the HIV-1 Protease Catalytic Aspartyl Groups Have Different Ionization States in the Complex Formed with the Asymmetric Drug KNI-272. *Biochemistry* **1996**, *35*, 9946-9950.

(33) Adachi, M.; Ohhara, T.; Kurihara, K.; Tamada, T.; Honjo, E.; Okazaki, N.; Arai, S.; Shoyama,

Y.; Kimura, K.; Matsumura, H.; Sugiyama, S.; Adachi, H.; Takano, K.; Mori, Y.; Hidaka, K.; Kimura, T.; Hayashi, Y.; Kiso, Y.; Kuroki, R. Structure of HIV-1 protease in complex with potent inhibitor KNI-272 determined by high-resolution X-ray and neutron crystallography. *Proc. Natl. Acad. Sci. USA* **2009**, *106*, 4641-4646.

(34) Weber, I. T.; Waltman, M. J.; Mustyakimov, M.; Blakeley, M. P.; Keen, D. A.; Ghosh, A. K.; Langan, P.; Kovalevsky, A. Y. Joint X-ray/Neutron Crystallographic Study of HIV-1 Protease with Clinical inhibitor Amprenavir: Insights for Drug Design. *J. Med. Chem.* **2013**, *56*, 5631-5635.

(35) Gerlits, O.; Wymore, T.; Das, A.; Shen, C-H.; Parks, J. M.; Smith, J. C.; Weiss, K. L.; Keen, D. A.; Blakeley, M. P.; Louis, J. M.; Langan, P.; Weber, I. T.; Kovalevsky, A. Long-Range Electrostatics-Induced Two-Proton Transfer Captured by Neutron Crystallography in an Enzyme Catalytic Site. *Angew. Chem. Int. Ed.* **2016**, *55*, 4924-4927.

(36) Chen, X.; Tropsha, A. Relative binding Free Energies of Peptide Inhibitors of HIV-1 Protease: The Influence of the Active Site Protonation State. *J. Med. Chem.* **1995**, *38*, 42-48.

(37) Tawa, G. J.; Topol, I. A.; Burt, S. K.; Erickson, J. W. Calculation of Relative Binding Free Energies of Peptide Inhibitors to HIV-1 Protease and Its I84V Mutant. *J. Am. Chem. Soc.* **1998**, *120*, 8856-8863.

(38) Rick, S. W.; Topol, I. A.; Erickson, J. W.; Burt, S. K. Molecular mechanisms of resistance: Free energy calculations of mutation effects on inhibitor binding to HIV-1 protease. *Protein Sci.*

1998, *7*, 1750-1756.

(39) Piana, S.; Sebastiani, D.; Carloni, P.; Parrinello, M. Ab Initio Molecular Dynamics-Based Assignment of the Protonation State of Pepstatin A/HIV-1 Protease Cleavage Site. *J. Am. Chem. Soc.* **2001**, *123*, 8730-8737.

(40) Nam, K-Y.; Chang, B. H.; Han, C. K.; Ahn, S. K.; No, K. T. Investigation of the Protonated State of HIV-1 Protease Active Site. *Bull. Korean Chem. Soc.* **2003**, *24*, 817-823.

(41) Zoete, V.; Michielin, O.; Karplus, M. Protein-ligand binding free energy estimation using molecular mechanics and continuum electrostatics. Application to HIV-1 protease inhibitors. *J. Comput. Aided Mol. Des.* **2003**, *17*, 861-880.

(42) Lepšík, M.; Kříž Z.; Havlas, Z. Efficiency of a Second-Generation HIV-1 Protease Inhibitor Studied by Molecular Dynamics and Absolute Binding Free Energy Calculations. *Proteins: Struc. Funct. Bioinf.* **2004**, *57*, 279-293.

(43) Ode, H.; Matsuyama, S.; Hata, M.; Hoshino, T.; Kakizawa, J.; Sugiura, W. Mechanism of Drug Resistance Due to N88S in CRF01_AE HIV-1 Protease, Analyzed by Molecular Dynamics Simulations. *J. Med. Chem.* **2007**, *50*, 1768-1777.

(44) Czodrowski, P.; Sotriffer, C. A.; Klebe, G. Atypical Protonation States in the Active Site of HIV-1 Protease: A Computational Study. *J. Chem. Inf. Model.* **2007**, *47*, 1590-1598.

(45) Wittayanarakul, K.; Hannongbua, S.; Feig, M. Accurate Prediction of Protonation State as a

Prerequisite for Reliable MM-PB(GB)SA Binding Free Energy Calculations of HIV-1 Protease Inhibitors. *J. Comput. Chem.* **2008**, *29*, 673-685.

(46) Chen, J.; Yang, M.; Hu, G.; Shi, S.; Yi, C.; Zhang, Q. Insights into the functional role of protonation states in the HIV-1 protease-BEA369 complex: molecular dynamics simulations and free energy calculations. *J. Mol. Model.* **2009**, *15*, 1245-1252.

(47) Kar, P.; Knecht, V. Energetic basis for drug resistance of HIV-1 protease mutants against amprenavir. *J. Comput. Aided. Mol. Des.* **2012**, *26*, 215-232.

(48) Yang, M.; Jiang, X.; Jiang, N. Protonation state and free energy calculation of HIV-1 protease-inhibitor complex based on electrostatic polarization effect. *Mol. Phys.* **2014**, *112*, 1659-1669.

(49) McGee, Jr., T. D.; Edwards, J.; Roitberg, A. E. pH-REMD Simulations Indicate That the Catalytic Aspartates of HIV-1 Protease Exist Primarily in a Monoprotonated State. *J. Phys. Chem. B* **2014**, *118*, 12577-12585.

(50) Bastys, T.; Gapsys, V.; Doncheva, N.; Kaiser, R.; de Groot, B. L.; Kalinina, O. V. Consistent Prediction of Mutation Effect on Drug Binding in HIV-1 Protease Using Alchemical Calculations. *J. Chem. Theory Comput.* **2018**, *14*, 3397-3408.

(51) Weber, I. T.; Harrison, R. W. Molecular mechanics analysis of drug-resistant mutants of HIV protease. *Protein Eng.* **1999**, *12*, 469-474.

(52) Chen, X.; Weber, I. T.; Harrison, R. W. Molecular dynamics simulation of 14 HIV protease mutants in complex with indinavir. *J. Mol. Model.* **2004**, *10*, 373-381.

(53) Zhang, J.; Hou, T.; Wang, W.; Liu, J. S. Detecting and understanding combinational mutation patterns responsible for HIV drug resistance. *Proc. Natl. Acad. Sci.* **2010**, *107*, 1321-1326.

(54) Leonis, G.; Steinbrecher, T.; Papadopoulos, M. G. A Contribution to the Drug Resistance Mechanism of Darunavir, Amprenavir, Indinavir, and Saquinavir Complexes with HIV-1 Protease Due to Flap Mutation I50V: A Systematic MM-PBSA and Thermodynamic Integration Study. *J. Chem. Inf. Model.* **2013**, *53*, 2141- 2153.

(55) Ota, R.; So, K.; Tsuda, M.; Higuchi, Y.; Yamashita, F. Prediction of HIV drug resistance based on the 3D protein structure: Proposal of molecular field mapping. *PLoS ONE* **2021**, *16*, e0255693-e0255707.

(56) Sohraby, F.; Aryapour, H. Comparative analysis of the unbinding pathways of antiviral drug Indinavir from HIV and HTLV1 proteases by supervised molecular dynamics simulation. *PLoS ONE* **2021**, *16*, e0257916-e0257925.

(57) Kosugi, T.; Hayashi, S. QM/MM Reweighting Free Energy SCF for Geometry Optimization on Extensive Free Energy Surface of Enzymatic Reaction. *J. Chem. Theory Comput.* **2012**, *8*, 322-334.

(58) Hayashi, S; Uchida, Y.; Hasegawa, T.; Higashi, M.; Kosugi, T.; Kamiya, M. QM/MM

Geometry Optimization on Extensive Free-Energy Surfaces for Examination of Enzymatic

Reactions and Design of Novel Functional Properties of Proteins. *Annu. Rev. Phys. Chem.* **2017**, *68*, 135-154.

(59) Kosugi, T.; Hayashi, S. Crucial Role of Protein Flexibility in Formation of a Stable Reaction

Transition State in an α-Amylase Catalysis. *J. Am. Chem. Soc.* **2012**, *134*, 7045-7055.

(60) Kato, H.; Kamiya, M.; Sugo, S.; Ito, J.; Taniguchi, R.; Orito, A.; Hirata, K.; Inutsuka, A.;

Yamanaka, A.; Maturana, A. D.; Ishitani, T.; Sudo Y.; Hayashi, S.; Nureki, O. Atomistic design

of microbial opsin-based blue-shifted optogenetics tools. *Nat. Commun.* **2015**, *6*, 7177-7186.

(61) Cheng, C.; Kamiya, M.; Uchida, Y.; Hayashi, S. Molecular Mechanism of Wide

Photoabsorption Spectral Shifts of Color Variants of Human Cellular Retinol Binding Protein II.

J. Am. Chem. Soc. **2015**, *137*, 13362-13370.

(62) Kamiya, M.; Hayashi, S. Photoactivation Intermediates of a G-Protein Coupled Receptor

Rhodopsin Investigated by a Hybrid Molecular Simulation. *J. Phys. Chem. B* **2017**, *121*, 3842-3852.

(63) Cheng, C.; Kamiya, M.; Takemoto, M.; Ishitani, R.; Nureki, O.; Yoshida, N.; Hayashi, S. An

Atomistic Model of a Precursor State of Light-Induced Channel Opening of Channelrhodopsin.

Biophys. J. **2018**, *115*, 1281-1291.

(64) Oda, K.; Nomura, T.; Nakane, T.; Yamashita, K.; Inoue, K.; Ito, S.; Vierock, J.; Hirata, K.; Maturana, A. D.; Katayama, K.; Ikuta, T.; Ishigami, I.; Izume, T.; Umeda, R.; Eguma, R.; Oishi, S.; Kasuya, G.; Kato, T.; Kusakizako, T.; Shihoya, W.; Shimada, H.; Takatsuji, T.; Takemoto, M.; Taniguchi, R.; Tomita, A.; Nakamura, R.; Fukuda, M.; Miyauchi, H.; Lee, Y.; Nango, E.; Tanaka, R.; Tanaka, T.; Sugahara, M.; Kimura, T.; Shimamura, T.; Fujiwara, T.; Yamanaka, Y.; Owada, S.; Joti, Y.; Tono, K.; Ishitani, R.; Hayashi, S.; Kandori, H.; Hegemann, P.; Iwata, S.; Kubo, M.; Nishizawa, T.; Nureki, O. Time-resolved serial femtosecond crystallography reveals early structural changes in channelrhodopsin. *eLife.* **2021**, *10*, e62389-e62419.

(65) Wang, J.; Wolf, R. M.; Caldwell, J. W.; Kollman, P. A.; Case, D. A. Development and testing of a general amber force field. *J. Comp. Chem.* **2004**, *25*, 1157-1174.

(66) Vanommeslaeghe, K.; Hatcher, E.; Acharya, C.; Kundu, S.; Zhong, S.; Shim, J.; Darian, E.; Guvench, O.; Lopes, P.; Vorobyov, I.; MacKerell Jr., A. D. CHARMM general force field: A force field for drug-like molecules compatible with the CHARMM all-atom additive biological force fields. *J. Comput. Chem.* **2010**, *31*, 671-690.

(67) Steinbrecher, T.; Mobley, D.L.; Case, D. A. Nonlinear scaling schemes for Lennard-Jones interactions in free energy calculations. *J. Comp. Chem.* **2007**, *127*, 214108-214120.

(68) Boyce, S. E.; Mobley, D. L.; Rocklin, G. J.; Gravers, A. P.; Dill, K. A.; Shoichet, B. K. Predicting Ligand Binding Affinity with Alchemical Free Energy Methods in a Polar Model Binding Sit. *J. Mol. Biol.* **2009**, *394*, 747-763.

(69) Chodera, J. D.; Mobley, D. L.; Shirts, M. R.; Dixon, R. W.; Branson, K.; Pande, V. S. Alchemical free energy methods for drug discovery: Progress and challenges. *Curr. Opin. Struct. Biol.* **2012**, *21*, 150-160.

(70) Mobley, D. L.; Klimovich, P. V. Perspective: Alchemical free energy calculations for drug discovery. *J. Chem. Phys.* **2012**, *137*, 230901-230912.

(71) Wang, L.; Wu, Y.; Deng, Y.; Kim, B.; Pierce, L.; Krilov, G.; Lupyan, D.; Robinson, S.; Dahlgren, M. K.; Greenwood, J.; Romero, D. L.; Masse, C.; Knight, J. L.; Steinbrecher, T.; Beuming, T.; Damm, W.; Harder, E.; Sherman, W.; Brewer, M.; Waster, R.; Murcko, M.; Fyre, L.; Farid, R.; Lin, T.; Mobley, D. L.; Jorgensen, W. L.; Berne, B. J.; Friesner, R. A.; Abel, R. Accurate and Reliable Prediction of Relative Ligand Binding Potency in Prospective Drug Discovery by Way of a Modern Free-Energy Calculation Protocol and Force Field. *J. Am. Chem. Soc.* **2015**, *137*, 2695-2703.

(72) Liu, W.; Jia, X.; Wang, M.; Li, P.; Wang, X.; Hu, W.; Zheng, J.; Mei, Y. Calculations of the absolute binding free energies for *Ralstonia solanacearum* lectins bound with methyl-α-l-fucoside at

molecular mechanical and quantum mechanical/molecular mechanical levels. *RSC. Adv.* **2017**, *7*, 38570-38580.

(73) Oshima, H.; Re, S.; Sugita, Y. Prediction of Protein–Ligand Binding Pose and Affinity Using the gREST+FEP Method. *J. Chem. Inf. Model.* **2020**, *60*, 5382-5394.

(74) Lee, T.-S.; Allen, B. K.; Giese, T. J.; Guo, Z.; Li, P.; Lin, C.; McGee Jr., T. D.; Pearlman, D. A.; Radak, B. K.; Tao, Y.; Tsai, H.-C.; Xu, H.; Sherman, W.; York, D. M. Alchemical Binding Free Energy Calculations in AMBER20: Advances and Best Practices for Drug Discovery. *J. Chem. Inf. Model.* **2020**, *60*, 5595-5623.

(75) Schmidt, M. W.; Baldridge, K. K.; Boatz, J. A.; Elbert, S. T.; Gordon, M. S.; Jensen, J. H.; Koseki, S.; Matsunaga, N.; Nguyen, K. A.; Su, S.; Windus, T. L.; Dupuis, M.; Montgomery, Jr J. A. General atomic and molecular electronic structure system. *J. Comput. Chem.* **1993**, *14*, 1347-1363.

(76) Case, D. A.; Betz, R. M.; Cerutti, D. S.; Cheatham, III, T. E.; Darden T. A.; Duke, R. E.; Giese, T. J.; Gohlke, H.; Goetz, A. W.; Homeyer, N.; Izadi, S.; Janowski, P.; Kaus, J.; Kovalenko, A.; Lee, T. S.; LeGrand, S.; Li, P.; Lin, C.; Luchko, T.; Luo, R.; Madej, B.; Mermelstein, D.; Merz, K. M.; Monard, G.; Nguyen, H.; Nguyen, H. T.; Omelyan, I.; Onufriev, A.; Roe, D. R.; Roitberg, A.; Sagui, C.; Simmerling, C. L.; Botello-Smith, W. M.; Swails, J.; Walker, R. C.; Wang, J.; Wolf,

R. M.; Wu, X.; Xiao, L.; Kollman, P. A. **2016**, AMBER 2016, University of California, San Francisco.

(77) Salmon-Ferrer, R.; Götz, A. W.; Poole, D.; Le Grand, S..; Walker, R. C. Routine Microsecond Molecular Dynamics Simulations with AMBER on GPUs. 2. Explicit Solvent Particle Mesh Ewald. *J. Chem. Theory. Comput.* **2013**, *9*, 3878-3888.

(78) Case, D. A.; Ben-Shalom, I. Y.; Brozell, S. R.; Cerutti, D. S.; Cheatham, III, T. E.; Cruzeiro, V. W. D.; Darden T. A.; Duke, R. E.; Ghoreishi, D.; Gilson, M. K.; Gohlke, H.; Goetz, A. W.; Greene, D.; Harris, R.; Homeyer, N.; Huang, Y.; Izadi, S.; Kovalenko, A.; Kurtzman, T.; Lee, T. S.; LeGrand, S.; Li, P.; Lin, C.; Liu, J.; Luchko, T.; Luo, R.; Mermelstein, D. J.; Merz, K. M.; Miao, Y.; Monard, G.; Nguyen, C.; Nguyen, H.; Omelyan, I.; Onufriev, A.; Pan, F.; Qi, R.; Roe, D. R.; Roitberg, A.; Sagui, C.; Schott-Verdugo, S.; Shen, J.; Simmerling, C. L.; Smith, J.; Salomon-Ferrer, R.; Swails, J.; Walker, R. C.; Wang, J.; Wei, H.; Wolf, R. M.; Wu, X.; Xiao, L.; York, D. M.; Kollman, P. A. **2018**, AMBER 2018, University of California, San Francisco.

(79) Hu, H.; Lu, Z.; Parks, J. M.; Burger, S. K.; Yang, W. Quantum mechanics/molecular mechanics minimum free-energy path for accurate reaction energetics in solution and enzymes: Sequential sampling and optimization on the potential of mean force surface. *J. Chem. Phys.* **2008**, *128*, 034105-034122.

(80) Reiling, K., K.; Endres, N. F.; Dauber, D. S.; Craik, C. S.; Stroud, R. M. Anisotropic

Dynamics of the JE-2147-HIV Protease Complex: Drug Resistance and Thermodynamic Binding

Mode Examined in a 1.09 Å Structure. *Biochemistry* **2002**, *41*, 4582-4594.

(81) Kashuba, A. D. M.; Dyer, J. R.; Kramer, L. M.; Raasch, R. H.; Eron, J. J.; Cohen, M. S.

Antiretroviral-Drug Concentrations in Semen: Implications for Sexual Transmission of Human

Immunodeficiency Virus Type 1. *Antimicrob. Agents Chemother.* **1999**, *43*, 1817-1826.

(82) Griffin, L.; Annaert, P.; Brouwer, K. Influence of Drug Transport Proteins on

Pharmacokinetitics and Drug Interactions of HIV Protease Inhibitors. *J. Pharm. Sci.* **2011**, *100*,

3636-3654.

(83) Jorgensen, W. L.; Chandrasekhar, J.; Madura, J. D.; Impey, R. W.; Klein, M. L. Comparison

of simple potential functions for simulating liquid water. *J. Chem. Phys.* **1983**, *79*, 926-935.

(84) Maier, J. A.; Martinez, C.; Kasavajhala, K.; Wickstrom, L.; Hauser, K. E.; Simmerling, C.

ff14SB: Improving the Accuracy of Protein Side Chain and Backbone Parameters from ff99SB.

J. Chem. Theory. Comput. **2015**, *11*, 3696-3713.

(85) Joung, I. S.; Cheatham, III, T. E. Determination of Alkali and Halide Monovalent Ion

Parameters for Use in Explicitly Solvated Biomolecular Simulations. *J. Phys. Chem. B* **2008**, *112*,

9020-9041.

(86) Becke, A. D. Density-functional thermochemistry. III. The role of exact exchange. *J. Chem. Phys.* **1993**, *98*, 5648-5652.

(87) Grimme, S.; Antony, S.; Ehrlich, S.; Kreig, H. A consistent and accurate *ab initio* parametrization of density functional dispersion correction (DFT-D) for the 94 elements H-Pu. *J. Chem. Phys.* **2010**, *132*, 154104-150122.

(88) Zhao, Y.; Truhlar, D. G. The M06 suite of density functionals for main group thermochemistry, thermochemical kinetics, non-covalent interactions, excited states, and transition elements: Two new functionals and systematic testing of four M06-class functionals and 12 other functionals. *Theor. Chem. Acc.* **2008**, *120*, 215-241.

(89) Bennett, C. H. Efficient Estimation of Free Energy Differences from Monte Carlo Data. *J. Comput. Phys.* **1976**, *22*, 245-268.

(90) Shirts, M. R.; Bair, E.; Hooker, G.; Pande, V. S. Equilibrium Free Energies from Nonequilibrium Measurements Using Maximum-Likelihood Methods. *Phys. Rev. Lett.* **2003**, *91*, 140601-140604.

(91) Shirts, M. R.; Pande, V. S. Comparison of efficiency and bias of free energies computed by exponential averaging, the Bennett acceptance ratio, and thermodynamic integration. *J. Chem. Phys.* **2005**, *122*, 144107-144122.

(92) Heaslet, H.; Rosenfeld, R.; Giffin, M.; Lin, Y.-C.; Tam, K.; Torbett, B. E.; Elder, J. H.; McRee,

D. E.; Stout, C. D. Conformational flexibility in the flap domains of ligand-free HIV protease. *Acta Crystallogr. D Biol. Crystallogr.* **2007**, *63*, 866-875.

(93) Hornak, V.; Okur, A.; Rizzo, R. C.; Simmerling, C. HIV-1 protease flaps spontaneously open and reclose in molecular dynamics simulations. *Proc. Natl. Acad. Sci.* **2006**, *103*, 915-920.

(94) Soares, R. O.; Torres, P. H. M.; da Silva, M. L.; Pascutti, P. G. Unraveling HIV protease flaps dynamics by Constant pH Molecular Dynamics simulations. *J. Struct. Biol.* **2016**, *195*, 216-226.

(95) Jindal, G.; Warshel, A. Exploring the Dependence of QM/MM Calculations of Enzyme Catalysis on the Size of the QM Region. *J. Phys. Chem. B* **2016**, *120*, 9913-9921.

(96) Das, S.; Nam, K.; Major, D. T. Rapid Convergence of Energy and Free Energy Profiles with Quantum Mechanical Size in Quantum Mechanical-Molecular Mechanical Simulations of Proton Transfer in DNA. *J. Chem. Theory Comput.* **2018**, *14*, 1695-1705.

(97) Kulik, H. J. Large-scale QM/MM free energy simulations of enzyme catalysis reveal the influence of charge transfer. *Phys. Chem. Chem. Phys.* **2018**, *20*, 20650-20660.

(98) Mehmood, R.; Kulik, H. Both Configuration and QM Region Size Matter: Zinc Stability in QM/MM Models of DNA Methyltransferase. *J. Chem. Theory Comput.* **2020**, *16*, 3121-3134.

(99) Cui, Q.; Pal, T.; Xie, L. Biomolecular QM/MM Simulations: What Are Some of the "Burning Issues"?. *J. Phys. Chem. B* **2021**, *125*, 689-702.

(100) Humphrey, W.; Dalke, A.; Schulten, K. VMD: visual molecular dynamics. *J. Mol. Graphics*

1996, *14*, 33-38.
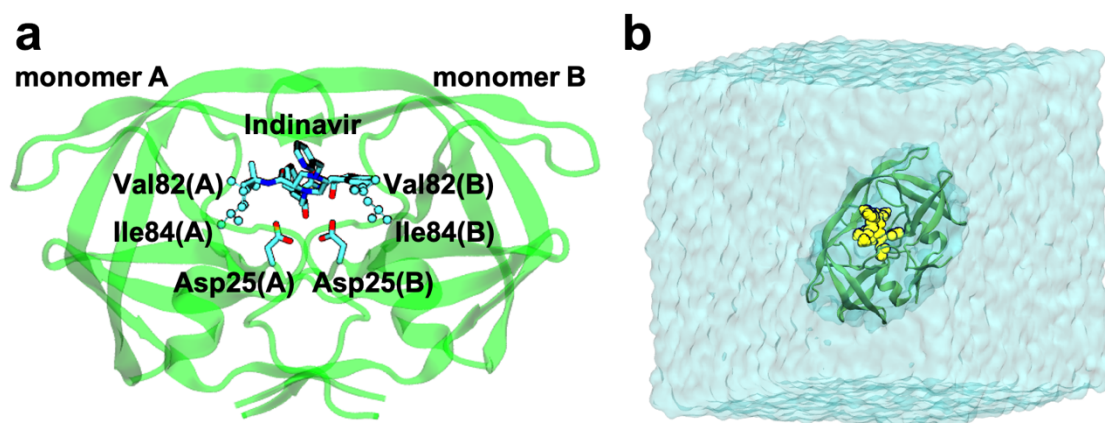
Figure 1. Structure of HIV-1 protease binding Indinavir and its molecular simulation system. **a** Structure of the wild-type HIV-1 protease binding Indinavir. The protein backbone is drawn in a ribbon representation. Heavy atoms of Indinavir and the sidechains of Asp25(A) and Asp25(B) in the monomers A and B, respectively, are depicted in a stick representation. Heavy atoms of the sidechains of Val82 and Ile84 are depicted in a ball and stick representation. **b** A QM/MM simulation system for the wild-type HIV-1 protease binding Indinavir in a water box in a periodic boundary condition. A quantum mechanically treated molecules are depicted in a van der Waals representation colored in *yellow*.
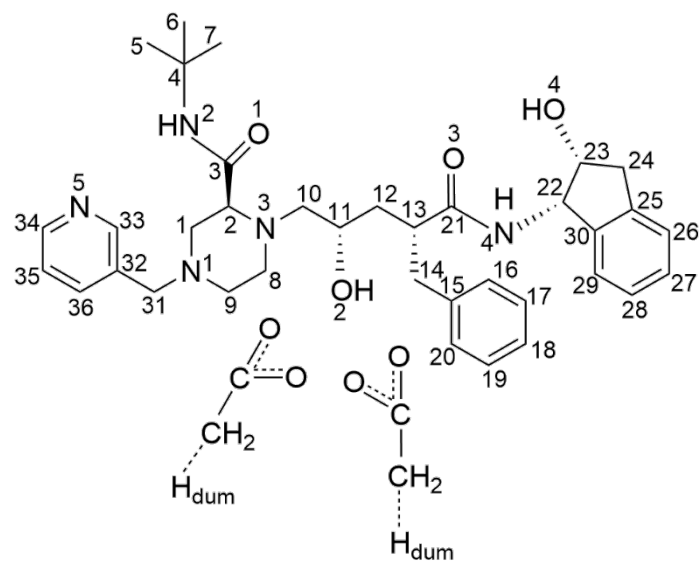
Figure 2. QM regions in the QM/MM RWFE-SCF calculations consisting of Indinavir and the sidechains of Asp25(A) and Asp25(B). Dummy hydrogen atoms to cap the QM regions, H$_{dum}$, are also shown.
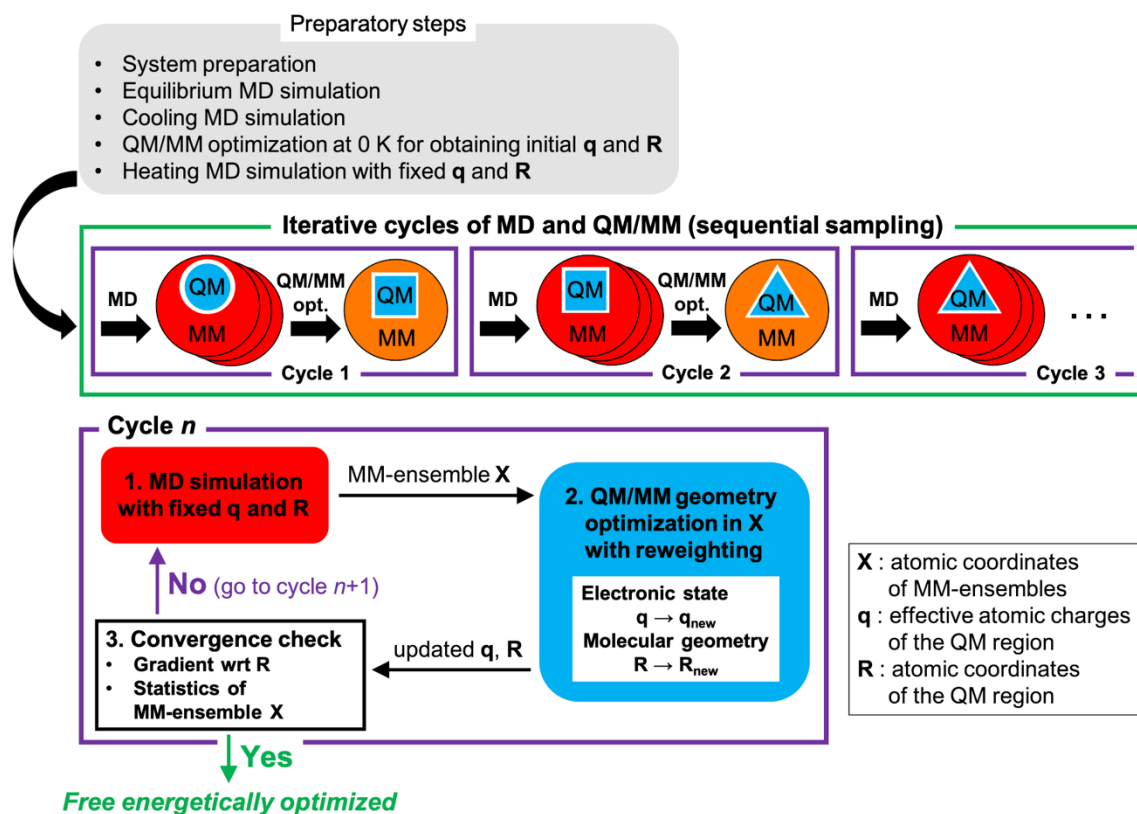
Figure 3. Calculation scheme of QM/MM RWFE-SCF free energy geometry optimization method. After preparatory steps where simulation systems are equilibrated and initial atomic coordinates **R** and effective atomic charges **q** of the QM region are obtained, iterative cycles of an MD sampling simulation and a QM/MM free energy geometry optimization shown in a green frame are performed. At each cycle shown in a purple frame, MD simulation with fixed **R** and **q** is firstly performed to statistically sample MM conformations **X**. Then, using the ensemble of the MM conformations **X**, a QM/MM free energy geometry optimization with a mean field approximation and reweighting is performed. By the QM/MM geometry optimization, **R** and **q** are updated for the MD sampling simulation of the next cycle. Finally, convergence of the overall free energy optimization is checked with a free energy gradient with respect to **R** and statistics of the ensemble of the MM conformations. The iterative cycles continue until the simultaneous convergences are achieved.
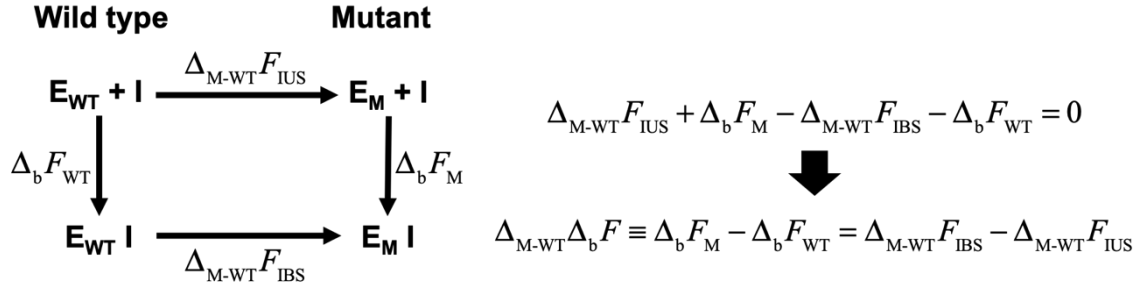
Figure 4. Alchemical free energy calculation scheme of a relative binding free energy between the wild-type enzyme (E_{WT}) binding with an inhibitor (I) and the mutant one (E_M). $\Delta_{M\text{-}WT}F_{IUS}$ is a free energy difference between the mutant enzyme and the wild-type one in the inhibitor unbound state (IUS), $\Delta_{M\text{-}WT}F_{IBS}$ is that in the inhibitor bound state (IBS), $\Delta_b F_{WT}$ is a free energy difference between the IBS and the IUS of the wild-type protein, and $\Delta_b F_M$ is that of the mutant. Simulations of the inhibitor in their unbound states of the wild-type and the mutant are not necessary because the free energies of the inhibitor in those unbound states where the inhibitor is released in bulk water are the same, and thus are canceled out when the free energy difference between the wild-type and the mutant is considered.
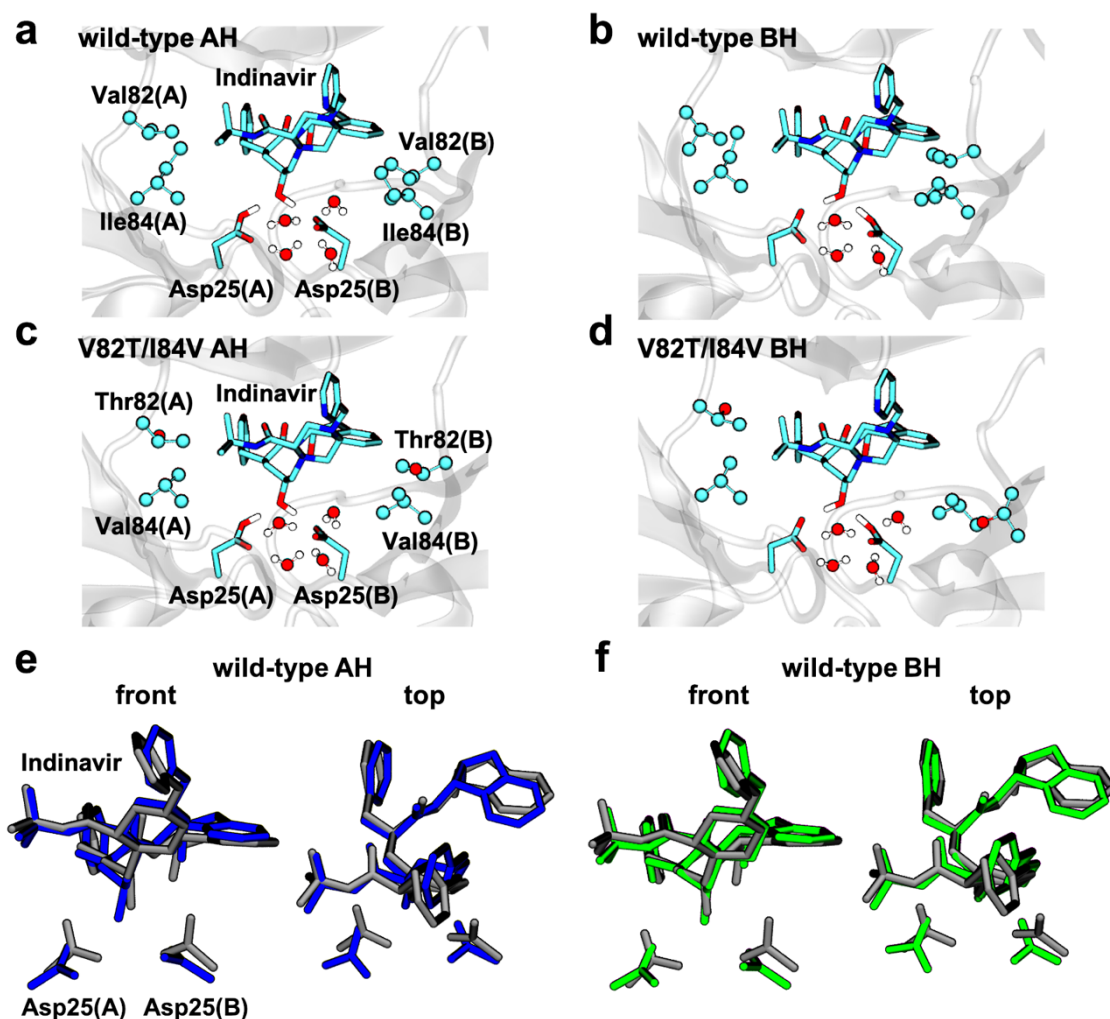
Figure 5. The free-energetically optimized structures obtained by the QM/MM RWFE-SCF calculations. **a** The wild-type structure in AH. **b** The wild-type one in BH. **c** The V82T/I84V mutant one in AH. **d** The V82T/I84V mutant one in BH with a fixed O-H distance of protonated Asp25(B). Heavy atoms of Indinavir and the sidechains of Asp25 are depicted in a stick representation. Water molecules within 3 Å of Asp25 and heavy atoms of the sidechains of Val82/Val82Thr and Ile84/Ile84Val are shown in a ball and stick representation. **e** Comparison between the optimized wild-type structure in AH (*blue*) and an X-ray crystallographic structure binding Indinavir (PDB ID: 1HSG) (*gray*). **f** Comparison between the optimized wild-type structure in BH (*green*) and the X-ray crystallographic one (*gray*). The heavy atoms of the optimized structures were RMSD-fitted to those of the X-ray crystallographic one.
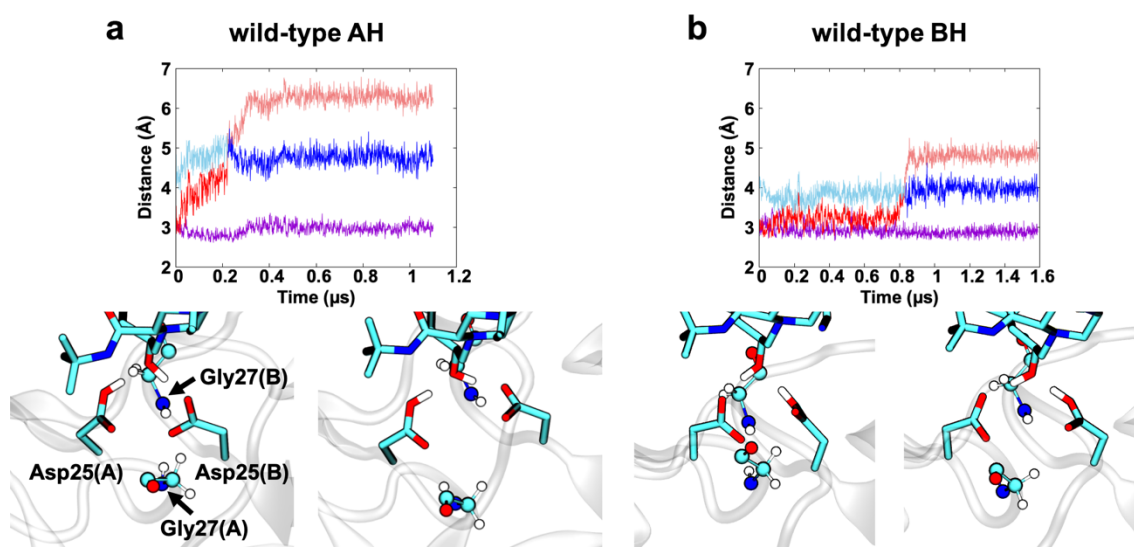
Figure 6. Temporal changes of distances between Asp25(A)/Asp25(B) and Gly27(A)/Gly27(B) during free energy optimizations. **a** The wild-type protein in AH. A distance between O_δ atom of the sidechain of Asp25(B) and N atom of the mainchain of Gly27(B) (*purple*), and those between O_δ atom of the sidechain of Asp25(B) and N atom of the mainchain of Gly27(A) (*red* and *blue*) are depicted. **b** The wild-type protein in BH. A distance between O_δ atom of the sidechain of Asp25(A) and N atom of the mainchain of Gly27(A) (*purple*), and those between O_δ atom of the sidechain of Asp25(A) and N atom of the mainchain of Gly27(B) (*red* and *blue*) are depicted. The distance and the angle including one of two O_δ atoms of Asp25 are colored in *red*, and those including the other are colored in *blue* in **a** and **b**. The distances of the O_δ atoms located farther from N atom of the mainchain of Gly27(A) are drawn in light colors. Bottom-left panels in **a** and **b** represent starting structures of free energy optimizations, respectively, and bottom-right ones represent the optimized ones. Heavy atoms of Indinavir and the sidechains of Asp25 are depicted in a stick representation. Gly27 are shown in a ball and stick representation.
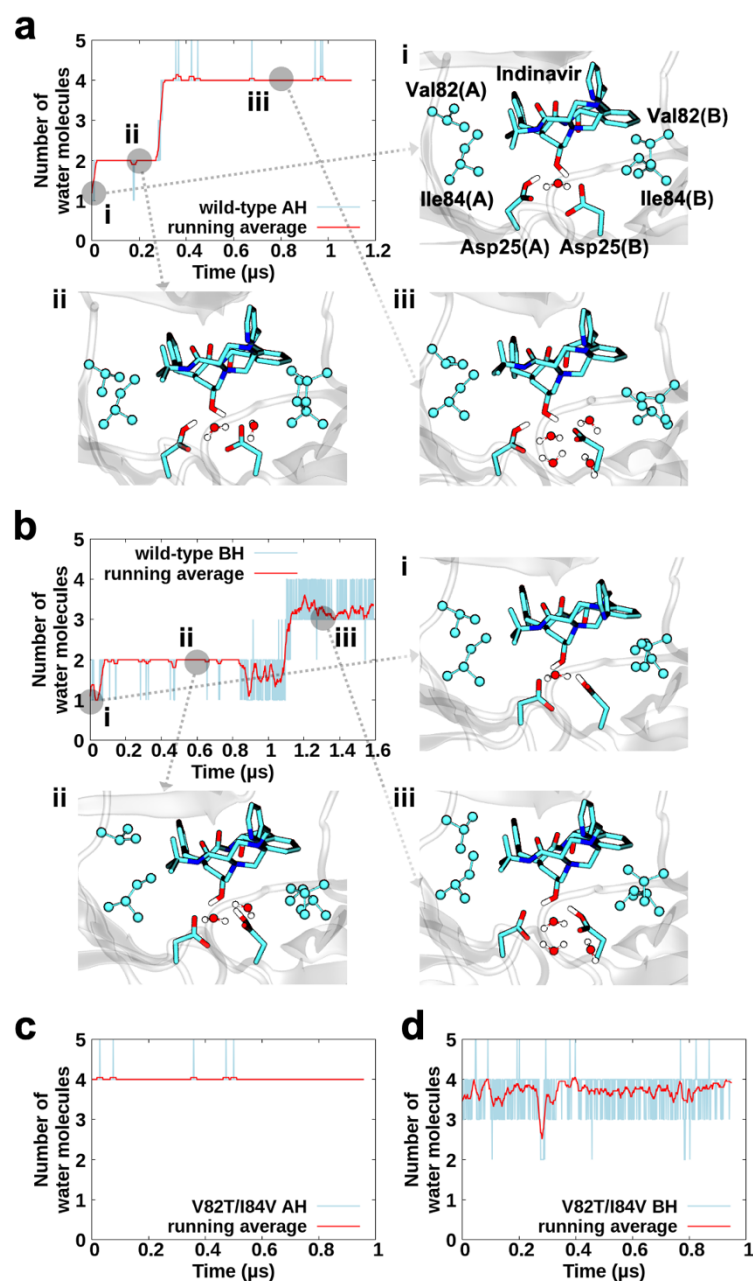
Figure 7. Temporal changes of the number of water molecules around Asp25 during the free energy optimizations. **a** The wild-type protein in AH. **b** The wild-type one in BH. **c** The V82T/I84V mutant in AH. **d** The V82T/I84V mutant in BH with a fixed O-H distance of protonated Asp25(B). Water molecules within 3 Å of Asp25(A) and Asp25(B) were counted. Window-averaged temporal changes are drawn with thick lines in *red*. Width of the averaging window is 20 ns. Snapshot structures of free energy optimizations are also shown in **a** and **b**. Heavy atoms of Indinavir and the sidechains of Asp25 are depicted in a stick representation. Water molecules within 3 Å of Asp25(A) and Asp25(B) and heavy atoms of sidechains of Val82 and Ile84 are shown in a ball and stick representation.
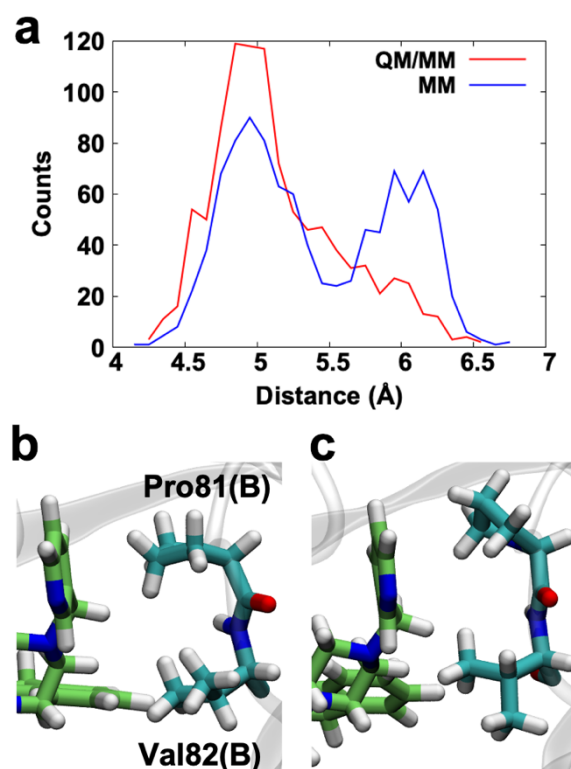
Figure 8. Hydrophobic interactions of the pyridyl group of Indinavir with the sidechains of Pro81(B) and Val82(B). **a** Distributions of distances between C_γ atom of Pro81(B) and C_β atom of Val82(B) in the QM/MM samples (*red*) and the MM ones (*blue*). The QM/MM samples were taken from a trajectory for 1 μs obtained by an MD simulation with the QM region of which the geometry and the effective atomic charges were fixed at the QM/MM free-energetically optimized ones with B3LYP-D3 functional. The MM samples were taken from the equilibrium MD simulation for 1 μs (see COMPUTATIONAL METHODS). A bin width of 0.1 Å was employed for the distributions. **b** A snapshot of the QM/MM samples where the distance in **a** is ~5 Å. Indinavir is depicted in *green*. **c** A snapshot of the MM samples where the distance in **a** is ~6 Å.
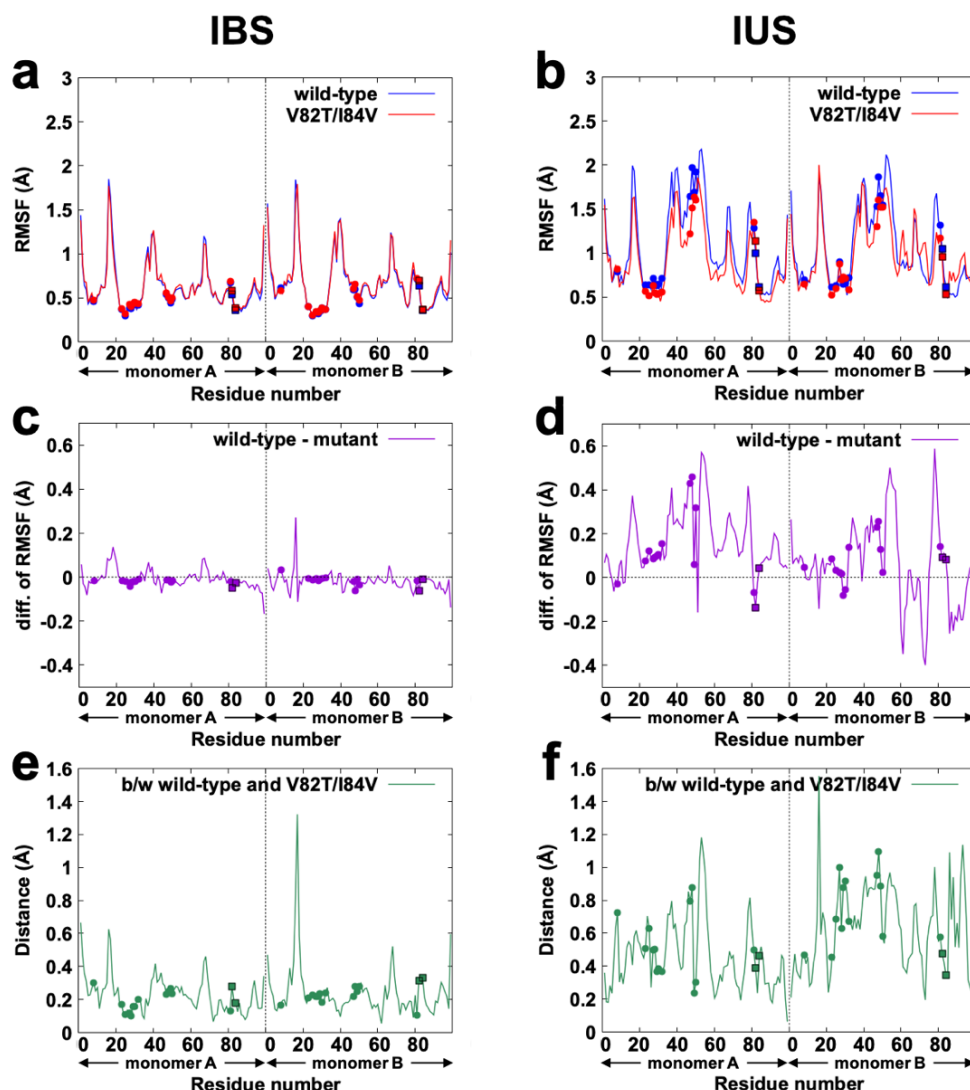
Figure 9. Structural comparison between the wild-type protein and the V82T/I84V mutant for IBS in the AH state and IUS. Conformational samples of IBS were taken from trajectories for 1 μs obtained by MD simulations with the QM region of which the geometry and the effective atomic charges were fixed at the QM/MM free-energetically optimized ones with B3LYP-D3 functional (see COMPUTATIONAL METHODS), and those of IUS were taken from equilibrium MD simulations for 1 μs. **a,b** C_α-RMSFs of IBS (**a**) and IUS (**b**) for wild-type protein (*blue*) and V82T/I84V mutant (*red*). Residues of which any heavy atoms are located within 4 Å of Indinavir (Arg8, Leu23, Asp25, Gly27, Ala28, Asp29, Asp30, Val32, Ile47, Gly48, Gly49, Ile50, Pro81) are marked by filled circles, and Val82(Thr82) and Ile84(Val84) are marked by filled squares. **c,d** Differences of the RMSFs of IBS (**c**) and IUS (**d**) between the wild-type protein and the V82T/I84V mutant. **e,f** C_α-distances of IBS (**e**) and IUS (f) between averaged structures of the wild-type protein and the V82T/I84V mutant of which positions of C_α atoms were averaged.

71

Table 1. Free Energy Differences between Two Mono-protonated States AH and BH, $\Delta_{\text{BH-AH}}F_{\text{QM/MM}}$, and Their Energy Components, $\Delta_{\text{BH-AH}}E_{\text{QM}}$ and $\Delta_{\text{BH-AH}}F_{\text{QM-MM,MM}}$, in kcal/mol.

	$\Delta_{\text{BH-AH}}E_{\text{QM}}$	$\Delta_{\text{BH-AH}}F_{\text{QM-MM,MM}}$	$\Delta_{\text{BH-AH}}F_{\text{QM/MM}}$
	Wild type		
Forward [a]	-18.1	20.7	2.6
Backward [b]	-18.1	21.1	3.0
Average [c]	-18.1	20.9	2.8
	V82T/I84V mutant		
Forward [a]	-13.2	18.1	4.9
Backward [b]	-13.2	17.5	4.3
Average [c]	-13.2	17.8	4.6

[a] Energy differences evaluated by forward samplings.

[b] Energy differences evaluated by backward samplings.

[c] Averages of energy differences evaluated by forward and backward samplings, respectively.

Table 2. Relative Binding Free Energies between the Wild-type Protein and the V82T/I84V

Mutant, $\Delta_{\text{M-WT}}\Delta_{\text{b}}F$, and Their Free Energy Components in kcal/mol.

QM/MM	$\Delta_{\text{M-WT(QM)}}E_{\text{QM}}$	$\Delta_{\text{M-WT(QM)}}F_{\text{QM-MM,MM}}$	$\Delta_{\text{M-WT}}F_{\text{alchemy}}$	$\Delta_{\text{M-WT}}F_{\text{IBS}}$	$\Delta_{\text{M-WT}}F_{\text{IUS}}$	$\Delta_{\text{M-WT}}\Delta_{\text{b}}F$
Forward [a]	1.7	-0.8	-12.1	-11.2	-15.1	3.9
Backward [b]	1.7	-2.4	-10.7	-11.4	-15.1	3.7
Average [c]	1.7	-1.6	-11.4	-11.3	-15.1	3.8
MM	$\Delta_{\text{M-WT}}F_{\text{IBS}}$	$\Delta_{\text{M-WT}}F_{\text{IUS}}$	$\Delta_{\text{M-WT}}\Delta_{\text{b}}F$			
Forward [a]	-14.4	-15.1	0.7			
Backward [b]	-15.2	-15.1	-0.1			
Average [c]	-14.8	-15.1	0.3			

[a] Energy differences evaluated by forward samplings.

[b] Energy differences evaluated by backward samplings.

[c] Averages of energy differences evaluated by forward and backward samplings, respectively.

Table of Contents Graphic

Structural modeling by
QM/MM RWFE-SCF method

wild type   V82T/I84V mutant

Indinavir
Val82(B)

+

Alchemical FEP framework

QM/MM   MM

Indinavir Val82(B)

$\Delta_{\text{M-WT}}\Delta_b F_{\text{QM/MM}}$
$= 3.8$ kcal/mol

$\Delta_{\text{M-WT}}\Delta_b F_{\text{MM}}$
$= 0.3$ kcal/mol

experimental value: 2.5~3.0 kcal/mol